Cavity-Enhanced Spectroscopy of Molecular Rare-earth-ion Complex

Master's Thesis
by

Weizhe Li

Matriculation number: 2440537

at the Karlsruhe School of Optics and Photonics (KSOP)

Reviewer:	Prof. Dr. David Hunger
Second Reviewer:	Prof. Dr. Wolfgang Wernsdorfer
Advisor:	M. Sc. Evgenij Vasilenko
Second Advisor:	Dr. Nicholas Lester Jobbitt

11. April 2023 - 11. October 2023

Karlsruher Institut für Technologie
Fakultät für Physik
Postfach 6980
76128 Karlsruhe

Declaration of Academic Integrity

I hereby confirm that the present thesis is solely my own work and that if any text passages or diagrams from books, papers, the Web or other sources have been copied or in any other way used, all references, including those found in electronic media, have been acknowledged and fully cited.

Karlsruhe, 11.10.2023

(Weizhe Li)

Acknowledgements

First I would like to thank Prof. Hunger for supervising this project and M. Sc. Vasilenko, as well as Dr. Jobbitt for advising me and proofreading the thesis. I am glad to have the chance to work in the group on quantum optics. I have learnt a lot during the six-month master's thesis. I also want to thank M. Sc. Timon Eichhorn, M. Sc. Jannis Hessenauer, Vishnu Unni C and all the people in the group for fruitful discussion and helpful support. It was an enjoyable time with the group. Also thanks to Max Planck School of Photonics for financing me with a scholarship and to KSOP for providing the Master program.

Abstract

Due to the electronic structure of the 4f-shell, rare-earth ions (REIs) have intrinsically long optical lifetimes and coherence times, which makes them good materials as gain media in lasers, and now, as optically addressable qubits in quantum technologies. Using molecular complexes as host material for REIs provides a new possibility to chemically engineer a favorable environment by tailoring the surrounding ligand fields of the REIs. This can tune the frequencies and branching ratios of transitions that are favorable for quantum technologieswhilst still maintaining good coherence times. Furthermore, multiple ions can be embedded into one molecule, enabling controllable coupling between the ions, which is essential for multi-qubit operation.

In this thesis, an Eu^{3+}-embedded molecular complex in the form of crystalline platelets is integrated into a fiber-based Fabry-Pérot microcavity in order to demonstrate cavity-enhanced spectroscopy. Using a recrystallization method, the crystalline platelets with thicknesses as low as 2 μm are grown on a planar cavity mirror. A number of crystals feature a RMS surface roughness of 0.4 nm on an area of 5 μm × 5 μm, corresponding to scattering loss of 100 ppm. Room temperature spectroscopy proves that the branching ratios, linewidths and optical lifetime are preserved during the recrystallization process.

With a laser-machined optical fiber, with controllable movement in the x-, y-, and z-dimensions through the use of piezos, the cavity can be scanned laterally in order to locate the crystals. A high-finesse cavity can be formed on most of the crystals, with a maximum finesse of 4,000. Cavity-enhanced fluorescence spectroscopy can be performed using an off-resonant excitation scheme. In the so-called bad emitter regime, where the effective Q-factor is determined via the Q-factor of the emitter, a Purcell factor of 0.09 is expected. The optical lifetime in the cavity is measured by off-resonant pulsed excitation, and is then compared with the free-space lifetime. At the present time, no conclusion can be made on the lifetime shortening in the cavity, because the lifetime difference lies within the statistic deviation. However, some individual cavity lifetimes show a reduction of about 10% compared to the free-space lifetime of 540 μs.

Contents

List of Figures ix

List of Tables xi

1 Introduction 1

2 Theoretical Background 3
- 2.1 Rare-earth Ion and Quantum Computing . . . 3
  - 2.1.1 Quantum Information Processing . . . 3
  - 2.1.2 Qubit Candidates . . . 4
  - 2.1.3 Rare-earth Ions as Qubits . . . 5
- 2.2 Fabry-Pérot Microcavity . . . 9
  - 2.2.1 Structure . . . 9
  - 2.2.2 Cavity Stability . . . 10
  - 2.2.3 Longitudinal Modes . . . 12
  - 2.2.4 Transverse Modes . . . 14
  - 2.2.5 Losses in the Cavity . . . 17
  - 2.2.6 Mode Dispersion and Hybridization . . . 19
  - 2.2.7 Characteristics of the Cavity . . . 23
  - 2.2.8 Fiber-based microcavity . . . 24
- 2.3 Purcell Enhancement . . . 24
  - 2.3.1 Models for Light-matter Interaction . . . 24
  - 2.3.2 Quantization of the Electromagnetic Field . . . 25
  - 2.3.3 Spontaneous Emission in a Fully Quantum Model . . . 27
  - 2.3.4 Cavity Enhancement and Purcell Factor . . . 28

3 Experimental Setup 31
- 3.1 Fiber-based Fabry-Pérot Scanning Microcavity . . . 31
  - 3.1.1 Fabrication of Cavity Fibers . . . 31
  - 3.1.2 Reflective Coating . . . 32
  - 3.1.3 Assembly of the Microcavity . . . 34

3.1.4 Optical Setup . . . 36
3.1.5 Active Stabilization . . . 37
3.2 Measurement Scheme . . . 38
3.2.1 Cavity Resonance Spectrum . . . 38
3.2.2 Cavity Scan . . . 38
3.2.3 Cavity Mode Dispersion . . . 40
3.3 Sample Preparation . . . 40
3.3.1 Molecular Structure . . . 40
3.3.2 Crystallization on Cavity Mirror . . . 40
3.3.3 Characterization of the Crystals . . . 41

4 Results and Discussion 45
4.1 Cavity Performance . . . 45
4.1.1 Scanning Cavity Microscopy of Molecular Crystals . . . 45
4.1.2 Mode Dispersion of a Hybrid Cavity . . . 47
4.1.3 Emission Dispersion . . . 48
4.2 Cavity Fluorescence Spectroscopy . . . 49
4.2.1 Double Resonance Condition . . . 49
4.2.2 Fluorescence Spectroscopy . . . 50
4.3 Measuring the Purcell Effect . . . 50
4.3.1 Estimation of the Purcell Factor . . . 50
4.3.2 Pulsed Excitation . . . 52
4.3.3 Lifetime Shortening . . . 52

5 Conclusion and Outlook 55

Bibliography 56

List of Figures

2.1 Energy level structure of an ^{151}Eu^{3+} ion embedded in a host material 5
2.2 Energy level diagram of a single Eu^{3+} ion 6
2.3 Calculated Zeeman splitting of Eu^{3+}:YSO 8
2.4 Sketch of a Fabry-Pérot cavity 10
2.5 Stability of a Fabry-Pérot cavity composed of two concave mirrors . 11
2.6 Cavity resonance spectra for different finesses 15
2.7 Intensity distribution of a Gaussian mode in free space 16
2.8 Intensity distribution of a Gaussian mode in cavity 17
2.9 Shapes of Hermite-Gaussian modes in the transverse plane 18
2.10 Cavity transmission signal while tuning the cavity length 19
2.11 Cavity mode dispersion of an empty cavity 20
2.12 Hybridized cavity modes 21
2.13 Simulated mode dispersion 22

3.1 Characterization of the fiber in the WLI 32
3.2 Reflectivity of a DBR depending on the number of stacks 33
3.3 Transmittance through DBRs with different coating layers 34
3.4 Mechanical structure of the fiber positioning setup 35
3.5 Mechanical structure of the mirror translation stage 36
3.6 A zoomed in picture of the microcavity taken by a microscope . . . 37
3.7 Optical setup for the cavity measurement 38
3.8 Cavity resonance spectrum on a clean part of the mirror 39
3.9 Cavity transmission maps 39
3.10 Structure of the molecular mononuclear Eu^{3+} complex 41
3.11 Crystal growth on a cavity mirror 41
3.12 Crystals under a microscope 42
3.13 Interference pattern and profile reconstruction 43
3.14 Fluorescence spectra of crystals from a confocal setup 43

4.1 Image of a crystal in the cavity 46
4.2 Scanning cavity microscopy on a crystal 46

4.3 Multi-channel scanning cavity microscopy 47
4.4 Mode dispersion of a hybrid cavity 48
4.5 Emission dispersion near 613 nm 49
4.6 Resonance spectrum of a two-color cavity 50
4.7 Fluorescence spectra of different longitudinal modes 51
4.8 The transient signal of the chopper wheel 53
4.9 Comparison of lifetimes in confocal setup and in cavity 54

List of Tables

2.1 Term symbols for different total orbital quantum numbers 6
2.2 Figures of merit for different applications with cavity 24

Chapter 1

Introduction

Quantum is everywhere. However, the quantum effects can mostly not be observed because the coherence, the soul of quantum, is lost due to various disturbances. That is why we are living in a so-called classical world.

Since the introduction of quantum theory, a lot of work has been done trying to observe quantum effects of individual quantum systems, which requires strong and coherent interaction with the system. The invention of the laser[1] provides a very useful tool for such a purpose. There are two approaches that can be taken. One is to reduce the interaction time such that no coherence can be lost during the interaction. Modern ultrafast laser techniques, based on high-order harmonic generation, can produce laser pulses with a duration in the range of attoseconds (as, 10^{-18} s), which can be used to capture fully coherent dynamics with high temporal resolution.[2]

The other direction is to preserve the coherence of the quantum system, for which a large number of techniques have been developed, including integration in cryogenic environment[3], ion trapping and radio-frequency driving[4]. Many different material platforms have been investigated for longer coherence time.

A coherent quantum system can be utilized in quantum information processing (QIP). Using quantum states as the computation units to store and process information, a quantum computer promise to be much faster and more efficient than a classical computer for particular tasks. In addition to long coherence times, a qubit is also required to be easy to address and scale up. With respect to recent research, promising candidates are trapped ions,[5, 6] Rydberg atoms,[7, 8], color centers in diamond,[9, 10] rare-earth ions in host materials[11, 12] and quantum dots.[13, 14]

Due to the electronic structure, the degeneracy in the 4f-shell of the REIs can be completely lifted, giving rise to abundant transitions with long coherence times for quantum technologies. In addition, the nuclear spin transitions resulting from the hyperfine interaction have even longer coherence times. An optical coherence time of 0.8 ms was measured in $^{171}\mathrm{Yb}^{3+}$:$\mathrm{Y_2SiO_5}$,[4] while the record nuclear spin coherence lifetime is 6 hours, measured in $^{151}\mathrm{Eu}^{3+}$:$\mathrm{Y_2SiO_5}$.[15] Recently, research has been focused on using organic molecular complexes as host materials[16–19], which provide a possibility to design the spectroscopic properties of the qubits and the interactions between them by chemically engineering the surrounding molecular environment of the REI. Recent research using diluted Eu^{3+}-embedded molecular complexes has proved an optical coherence time of 68 μs at 1.42 K.[17]

Like many other qubit candidates, the REIs also suffer from weak transition intensitiy. Therefore, a high coupling efficiency between the light and the REIs is required. A number of confining techniques have been developed, for example optical resonators[20–22] and photonic crystal structures.[23, 24]

A Fabry-Pérot microcavity[22, 25], consisting of mirrors with high reflectivities, can achieve high finesse and spatial resolution, which is an ideal tool to investigate quantum emitters in the form of crystals and particles. Based on such a microcavity, a scanning cavity microscope has been made,[26] which has been further utilized to measure Raman spectroscopy[27] and investigate the optical properties of diamond membranes.[28] In addition, such a platform is also capable for cryogenic operation.[29]

In this thesis, the non-diluted molecular complex described in Ref. [17] is integrated in the form of crystalline platelets into a fiber-based Fabry-Pérot microcavity by recrystallization while preserving the optical properties. Cavity operation and cavity-enhanced spectroscopy are demonstrated at room temperature.

The structure of this thesis is as follows. First, the theoretical background is discussed in chapter 2. Then, in chapter 3, the microcavity setup and the sample preparation method are introduced, followed by the measurement schemes. After this, the measurement results are presented and discussed. Finally, the work is summarized, followed by an outlook for future improvements.

Chapter 2

Theoretical Background

In this chapter, we introduce the theoretical background relevant to our research. We first describe the idea of quantum computing and the demands on qubits. Then we show the energy level structure of REIs in general and why the molecular complexes as host materials are special. From the optical side, we introduce the fiber-based Fabry-Pérot microcavity that we use to confine the light. Finally, combining emitters and an optical cavity, we introduce a quantum model for light-matter interaction and explain the Purcell effect.

2.1 Rare-earth Ion and Quantum Computing

Quantum computing is a new concept of information processing, which utilize quantum states to perform computation. A number of quantum systems and the corresponding schemes to address them have been investigated. As one of the candidates, REIs feature long optical and nuclear spin coherence times. Recently developed molecular complexes as the host materials make it possible to engineer the geometry between the quantum emitters and further extend the coherence times.

2.1.1 Quantum Information Processing

The modern digital computers are based on electronic devices. The information is processed as voltages in transistors. The voltage can change the property of the semiconductors, making them conducting or insulating. The computing speed depends on the speed of the electronic switch, which is limited by the speed of charge transfer in the semiconductors. This limits the clock rate to a maximum of a few GHz.

A quantum computer makes use of quantum states to perform computation. Rather than transistors, the computation units in a quantum computer are quantum systems called qubits. The simplest model for a qubit is a two-level system. The information is stored in the quantum states and manipulated by light, i.e. photons. A logic gate operation can be performed with two interacting qubits. For example, an excitation in one qubit will shift the transition of another qubit nearby, and thus activate or deactivate the transition. It is worth mentioning that in general, the qubit is not limited to atomic systems. A photon can also be a qubit, a so-called flying qubit.

A classical bit is a binary system with two states: on (1) and off (0). Although a qubit is still a two-level system, via coherent superposition, a real number can be stored in a qubit. Making use of the phase, a qubit can also process a complex number. From binary to complex, a quantum computer has much higher capacity compared to electronic computers. Not limited by the speed of the electronic switch, a quantum computer has the potential to be much faster and more efficient than electronic computers for may tasks.

2.1.2 Qubit Candidates

To benefit from the advantages of quantum computing, a number of criteria must be met. For fidelity, the qubits have to remain coherent until the computation is completed. But naturally, a quantum system is always coupled with the environment and thus tends to lose the coherence which is called decoherence. The time a quantum system can stay coherent is called the coherence time. A qubit has to be easily identified and distinguished from other qubits in order to write, process and read out the information precisely. Due to the weak dipole moments of the transitions, a high coupling efficiency is required, in order to address and read out the qubits precisely. Some confining techniques will be discussed in Sec. 2.2.

To find good candidates for qubits, a number of different material platforms have been recently explored. Examples are trapped ions,[5, 6] Ryderburg atoms,[7, 8], color centers in diamond,[9, 10] rare-earth ions in host materials[11, 12] and quantum dots.[13, 14]

The most straightforward way to create a qubit is to use a single atom or ion. However, as such atoms tend to be free moving, trapping is needed to extend the interaction time with the light. Alternatively, solid-state-based qubits are not free to move and thus can be easily located. However, they face a significant amount of ambient noise from the host materials. A large amount of work has been done to decouple the qubits from the environment, for example by cooling down the system, engineering the host materials and using dynamic decoupling sequences.

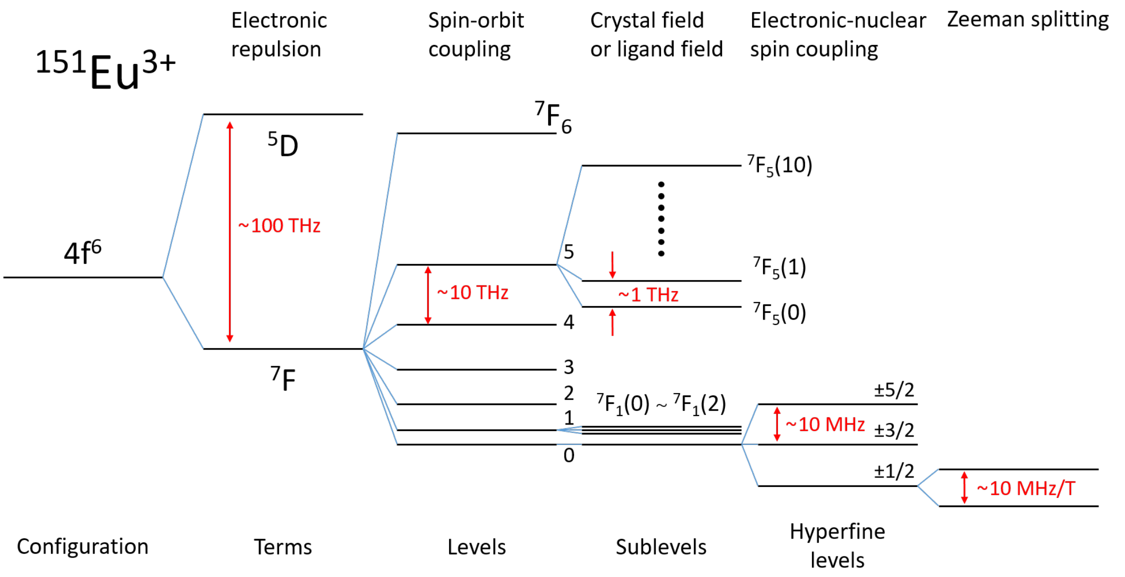
151Eu3+
Electronic repulsion
Spin-orbit coupling
Crystal field or ligand field
Electronic-nuclear spin coupling
Zeeman splitting
4f6
5D
7F
~100 THz
7F6
5
4
3
2
1
0
~10 THz
7F5(10)
7F5(1)
7F5(0)
~1 THz
7F1(0) ~ 7F1(2)
±5/2
±3/2
±1/2
~10 MHz
~10 MHz/T
Configuration
Terms
Levels
Sublevels
Hyperfine levels

Figure 2.1: **Energy level structure of an ^{151}Eu^{3+} ion embedded in a host material.** The isospin $I = 5/2$ gives rise to a zero-field triplet hyperfine structure.

2.1.3 Rare-earth Ions as Qubits

The rare-earth elements are composed of the group of lanthanides together with scandium, yttrium and lanthanum. They feature a special electronic structure which has partially filled 4f (for lanthanides), 4d (for yttrium) or 3d (for scandium) shells are located within the completely filled 5s and 5p shells, and thus are shielded from external electric fields. Therefore, the transitions within those shielded shells have long lifetime and coherence time.

REIs have multiple line-splitting mechanisms, including electronic repulsion, spin-orbit coupling and the hyperfine interaction. A large number of transitions are therefore available for quantum computing.

Energy Level Structure of Eu^{3+}

Here we take ^{151}Eu^{3+}, which is investigated in this work, as an example to explain the energy level structure of REIs in host materials. The electron configuration of Eu^{3+} can be written as [Xe]4f^6. To understand the energy level structure of Eu^{3+}, we will show how the degeneracy of the 4f^6-configuration is lifted step by step as shown in Fig. 2.1.

The 4f shell has 7 orbitals with degenerate energy for a single electron. However, when filled with electrons, the degeneracy is first lifted due to Coulomb repulsion

L	0	1	2	3	4	5	6	7	8	⋯
Symbol	S	P	D	F	G	H	I	K	L	⋯

Table 2.1: **Term symbols for different total orbital quantum numbers.** The first four symbols are derived from the characteristics of the lines corresponding to s, p, d, and f orbitals: sharp, principal, diffuse, and fundamental; the rest are named in alphabetical order from G onwards, omitting J, S and P.

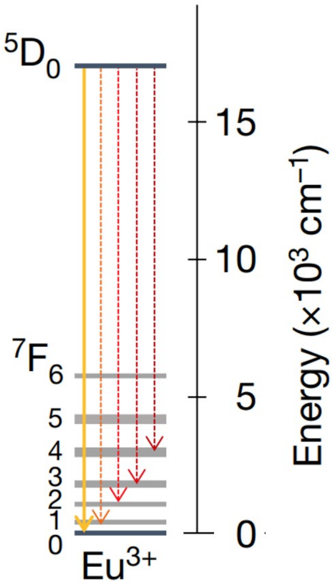

Figure 2.2: **Energy level diagram of a single Eu^{3+} ion.** The figure is adapted from Ref. [17].

between the electrons. Therefore, instead of the orbital quantum number l, the new good quantum numbers are the total electronic spin quantum number S and the total orbital quantum number L. The new eigenstates are called terms and denoted as ^{2S+1}L. Here L is represented by a symbol given in Tab. 2.1. The transitions between different terms are typically on the order of 100 THz.

Further, we have spin-orbit coupling, also called Russell–Saunders coupling[30] or LS-coupling, because quantum numbers L and S are coupled due to the interaction between the orbital angular momentum and the spin angular momentum. The energy is determined by the total angular momentum quantum number J, ranging from $|L - S|$ to $L + S$. Based on the term symbols, the levels are $^{2S+1}L_J$. With the spin-orbit coupling, a term is splitted into several levels and the transitions between them are typically on the order of 10 THz. In particular, the energy levels of a single Eu^{3+} ion are shown in Fig. 2.2.

So far, all the discussion is about a single ion. When an ion is doped into a crystal with a certain lattice structure or embedded into a molecule, the crystal field or the ligand field will affect the energy level structure of the ion, which are shifted and splits the energy levels into sublevels, lifting the degeneracy on the quantum number J. In this case, the quantum number is m_J, representing the projection of the total angular momentum, with the range from $-J$ to J. The sublevels are denoted as ${}^{2S+1}L_J(n)$, whereas $n = 0$ corresponds to the lowest energy level of the multiplet. The energy splitting caused by the crystal field or the ligand field is typically on the order of 1 THz and varies for different host materials. For crystal fields or ligand fields with the lowest symmetry, the $2J+1$ degeneracy is completely lifted.

In general, according to Laporte's selection rules[31], none of the intraconfigurational 4f-4f electric dipole transitions are allowed. However, when embedded into suitable host materials, those transitions become partially allowed due to crystal field effects. Therefore, they are often called induced electric dipole transitions. The selection rules of such transitions within the 4f-configuration are:[32]

$$\begin{aligned} &|\Delta S| = 0, \\ &|\Delta L| \leq 6, \\ &|\Delta J| \leq 6 \text{ and } |\Delta J| = 2,\ 4,\ 6 \text{ if } J = 0 \text{ or } J' = 0. \end{aligned} \tag{2.1}$$

The selection rules for ΔS and ΔL are not strictly valid, because S and L are not good quantum numbers any more. Rather the selection rule on J is more rigorous, but it can still relax by J-mixing[33]. Therefore, the ${}^5\mathrm{D}_0 \to {}^7\mathrm{F}_J$ (J=0, 3, 5) transitions have relatively low intensities.

With the interaction between the electronic and nuclear spins, the degeneracy on the nuclear isospin I is lifted. The magnetic dipole coupling, called IJ-coupling analogous to LS-coupling, together with the electric quadrupole coupling, gives rise to the hyperfine structure. For the two stable isotopes ^{151}Eu and ^{153}Eu, both with isospin $I = 5/2$, the three hyperfine levels have quantum numbers $m_I = \pm 1/2,\ \pm 3/2,\ \pm 5/2$, representing the projection of the nuclear isospin. The typical energy scale of such hyperfine splittings is on the order of 10 MHz, depending on the isotope. The hyperfine transitions are strictly forbidden, because no electric dipole is involved. Without disturbance from other nuclear spins, the lifetimes of the hyperfine states are much longer than the optical lifetimes.

The degeneracy between positive and negative m_I can be further lifted by an external magnetic field, which is the so-called Zeeman effect. The Landé g-factor of ${}^{151}\mathrm{Eu}^{3+}$ is on the order of 10 MHz/T.[34, 35] An example of calculated Zeeman splitting of Eu^{3+}:$\mathrm{Y_2SiO_5}$ (Eu^{3+}:YSO) is shown in Fig. 2.3. The Zeeman effect provides freedom to tune the hyperfine levels. The record nuclear spin coherence time of 6 hours is measured at a zero first order Zeeman (ZEFOZ) point in Eu^{3+}:YSO. [15]

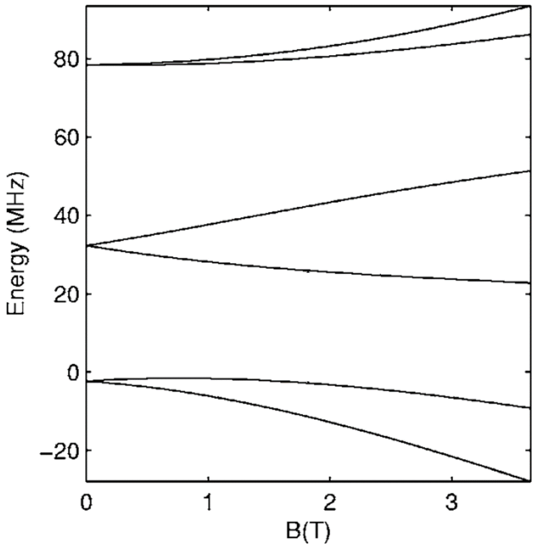

Figure 2.3: **Calculated Zeeman splitting of Eu^{3+}:YSO.** The figure is adapted from Ref. [34].

Host Materials

As discussed before, the host materials create a crystal field or ligand field to the REIs, which will lift the degeneracy on J. Most importantly, the host materials will relax the selection rules and activate some transitions which are usually forbidden.

Solid-state host materials have been extensively investigated, including Eu^{3+}:YSO, Eu^{3+}:Y_2O_3 and EuP_5O_{14}. These materials can be synthesised as bulk crystals with good optical properties, for example low scattering. In addition, they can be made into nanoparticles while maintaining the good optical properties in order to reduce the density of emitters in a single particle to address single emitters.

However, the provided environment is not quiet enough to fully exploit REI properties. In addition, the distance between emitters in the solid-state materials is not controllable, since doping is a stochastic process.

Some recently studied host materials are organic molecular complexes. Rather than the solid-state host materials, each ion in the molecular complexes has exactly the same environment because the molecules are identical. The structure of a molecular complex can be easily engineered. By changing the symmetry of the molecule, the transition dipole moment can be modified, and thus the transition amplitudes. Two or more REIs can also be embedded into one molecule with distinct distance and geometry to control the interaction between the ions and even to achieve multi-qubit coupling.

In this research, we prove that organic molecular complex recently reported in Ref.[17] can also form thin and smooth crystalline platelets, which are favourable for cavity integration. It is shown that our method of preparation preserves the optical properties during the crystallization process.

2.2 Fabry-Pérot Microcavity

In order to perform qubit manipulation, light is used to interact with an individual qubit, in the case of REIs, a single ion. To increase the excitation and detection efficiency, the interaction between light and matter has to be enhanced. One of the solutions is to confine the photons to a small volume close to the emitters for as long as possible. Various techniques for this purpose have been developed,[36] for example optical resonators,[20–22] ion traps[37, 38] and photonic crystals.[23, 24]

In this research, a high-finesse Fabry-Pérot microcavity is used to confine the photons, with a potential to achieve sub-λ^3 volume. Additional to quantum computing, such a microcavity can also be used to track and trap nanoparticles,[39, 40] sense the refractive index of the cavity medium,[41] and investigate cavity quantum electrodynamics.[42]

2.2.1 Structure

A Fabry-Pérot cavity (FPC), also called a Fabry-Pérot interferometer or etalon, is an optical cavity composed of two parallel mirrors used to trap the photons inside. Such a cavity was first developed by Charles Fabry and Alfred Perot[1] in 1899.[43, 44] In addition to optics, the FPC is also widely used in other fields, for example telecommunication and astronomy, to measure, filter and stabilize optical frequencies.

As shown in Fig. 2.4, the simplest FPC is composed of two planar mirrors separated by a distance l, with reflection coefficients r_1 and r_2, respectively. Without loss of generality, the reflection coefficients can be assumed to be real and positive, as the reflection phases are constant phase shifts added to each round trip. E_m represents the electric field amplitude of the light in the cavity after the m^{th} round trip. The total amplitude in the cavity can then be calculated:

$$E_{\mathrm{c}} = \sum_{m=0}^{\infty} E_m = \sum_{m=0}^{\infty} \left(r_1 r_2 e^{-i\varphi}\right)^m E_0, \tag{2.2}$$

where $\varphi = \frac{4\pi n l \nu}{\mathrm{c}}$ is the propagation phase, with n the refractive index of the cavity medium, ν the frequency of the light and c the speed of light in vacuum. As a

---

[1] His last name is spelt Perot but he used Pérot in publications.

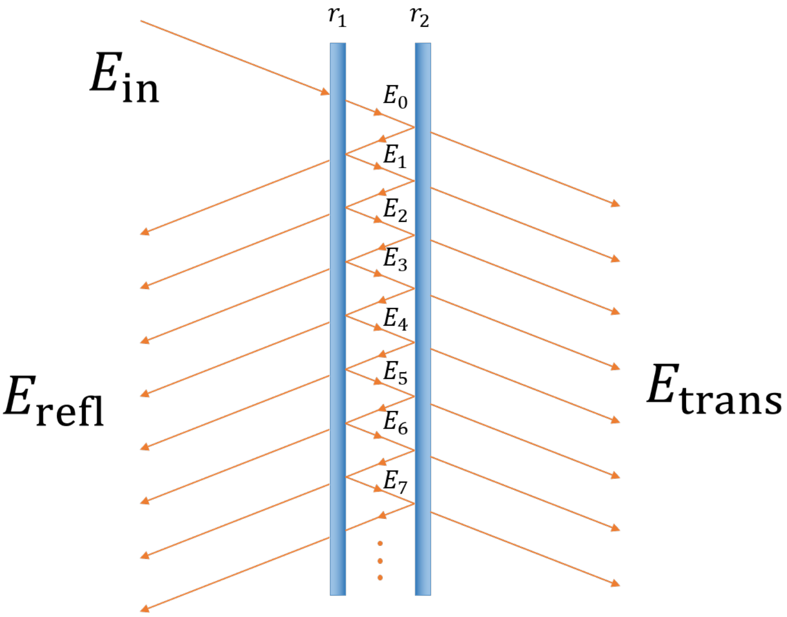

Figure 2.4: **Sketch of a Fabry-Pérot cavity.**

geometric series, Eq. (2.2) can be easily simplified as:

$$E_c = \frac{E_0}{1 - r_1 r_2 e^{-i\varphi}}. \tag{2.3}$$

To describe how much power is trapped in the cavity, the cavity enhancement factor A_c is defined as the power ratio between the trapped and input light:

$$A_c \equiv \frac{P_c}{P_{\text{in}}} = \frac{|E_c|^2}{|E_{\text{in}}|^2} = \frac{|E_0|^2}{|E_{\text{in}}|^2} \frac{1}{|1 - r_1 r_2 e^{-i\varphi}|^2} = \frac{T_1}{1 + R^2 - 2R\cos\varphi}, \tag{2.4}$$

where T_1 is the transmittance, or power transmission coefficient of the left mirror. For simplicity, in the last step, the mean reflectance, or power reflection coefficient, $R = r_1 r_2$ is used. In practice, the cavity transmittance:

$$T_c = T_2 A_c = \frac{T_1 T_2}{1 + R^2 - 2R\cos\varphi} \tag{2.5}$$

is used, where T_2 is the transmittance of the right mirror.

2.2.2 Cavity Stability

For a stable cavity, a beam should converge after infinite round trips. Mathematically, a ray transfer matrix, or ABCD matrix, can be used to describe a optical

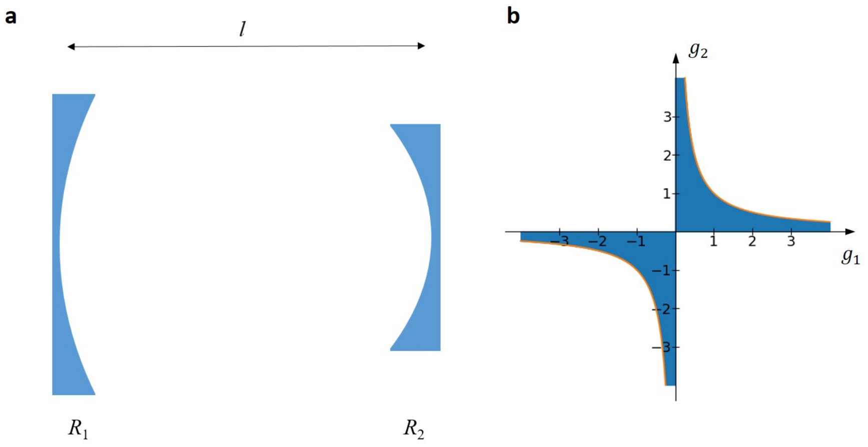

Figure 2.5: **Stability of a Fabry-Pérot cavity composed of two concave mirrors.** **a**: The sketch of such a cavity. **b**: Stability diagram of such a two-mirror cavity. A stable cavity can be formed if the parameters (g_1, g_2) fall into the blue region.

system. Consider a cavity shown in Fig. 2.5a composed of two concave mirrors separated by a distance l, with radii of curvature R_1 and R_2 (negative for convex mirrors), respectively. The ray transfer matrix for a round trip in such a cavity is

$$\begin{aligned}\mathbf{T} &= \begin{pmatrix} 1 & 0 \\ -\frac{2}{R_1} & 1 \end{pmatrix} \begin{pmatrix} 1 & l \\ 0 & 0 \end{pmatrix} \begin{pmatrix} 1 & 0 \\ -\frac{2}{R_2} & 1 \end{pmatrix} \begin{pmatrix} 1 & l \\ 0 & 0 \end{pmatrix} \\ &= \begin{pmatrix} 1 & l \\ -\frac{2}{R_1} & 1-\frac{2l}{R_1} \end{pmatrix} \begin{pmatrix} 1 & l \\ -\frac{2}{R_2} & 1-\frac{2l}{R_2} \end{pmatrix} \\ &= \begin{pmatrix} 1-\frac{l}{R_2} & 2l-\frac{2l^2}{R_2} \\ -\frac{2}{R_1}-\frac{2}{R_2}+\frac{4l}{R_1R_2} & -\frac{2l}{R_2}+\left(1-\frac{2l}{R_1}\right)\left(1-\frac{2l}{R_2}\right) \end{pmatrix}.\end{aligned} \tag{2.6}$$

The eigenvalues of a matrix $\mathbf{A}$ have the following properties:

$$\mathrm{tr}(\mathbf{A}) = \sum_i \lambda_i \tag{2.7}$$

and

$$\det(\mathbf{A}) = \prod_i \lambda_i, \tag{2.8}$$

with λ_i being the i^{th} eigenvalue of $\mathbf{A}$.

In the case of the ray transfer matrix in Eq. (2.6), we have

$$\lambda_1 + \lambda_2 = \mathrm{tr}(\mathbf{T}) = 4\left(1-\frac{l}{R_1}\right)\left(1-\frac{l}{R_2}\right) - 2 \tag{2.9}$$

and

$$\lambda_1\lambda_2 = \det(\mathbf{T}) = 1. \tag{2.10}$$

In order to have a stable cavity, it is required that

$$\max\{|\lambda_1|, |\lambda_2|\} \leq 1. \tag{2.11}$$

This is only true when:

$$\lambda_1 = \mathrm{e}^{i\phi}, \lambda_2 = \mathrm{e}^{-i\phi}. \tag{2.12}$$

Following this

$$\lambda_1 + \lambda_2 = 2\cos\phi, \tag{2.13}$$

therefore

$$-2 \leq 4\left(1 - \frac{l}{R_1}\right)\left(1 - \frac{l}{R_2}\right) - 2 \leq 2. \tag{2.14}$$

We obtain that the stability condition of such a cavity is

$$0 \leq \left(1 - \frac{l}{R_1}\right)\left(1 - \frac{l}{R_2}\right) \leq 1. \tag{2.15}$$

$g_1 \equiv 1 - \frac{l}{R_1}$ and $g_2 \equiv 1 - \frac{l}{R_2}$ are called the stability parameters. In the stability diagram shown in Fig. 2.5b, the region where a stable cavity is formed is colored blue.

2.2.3 Longitudinal Modes

Qualitatively, the cavity is on resonance when the propagation phase during a round trip is a multiple of 2π such that:

$$\varphi = \frac{4\pi n l \nu}{\mathrm{c}} = 2\pi q, \tag{2.16}$$

where q is a positive integer. This is also obvious that when the resonance condition is fulfilled, the cavity transmittance in Eq. (2.5) reaches the maximum

$$T_{\mathrm{c,max}} = \frac{T_1 T_2}{(1-R)^2}. \tag{2.17}$$

If the cavity length is fixed, then the q^{th} order resonance frequency is given by

$$\nu_q = \frac{q\mathrm{c}}{2nl}. \tag{2.18}$$

Whereas, if the frequency is fixed, then the q^{th}' order resonance cavity length is given by

$$l_q = \frac{q\mathrm{c}}{2n\nu}. \tag{2.19}$$

Based on Eq. (2.18), we can define the free spectral range (FSR) as the distance between two neighbouring resonance frequencies:

$$\Delta\nu = \frac{\mathrm{c}}{2nl}, \tag{2.20}$$

which is also the frequency of a photon bouncing back and forth in the cavity. Considering the FSR of wavelength, we get another useful expresion:

$$\Delta\lambda = \frac{\lambda^2}{2nl}. \tag{2.21}$$

When A_c decreases to half of the maximum, we have

$$1 + R^2 - 2R\cos\varphi = 2\left(1 - R\right)^2. \tag{2.22}$$

Thus, φ has to fulfill:

$$\cos\varphi = 1 - \frac{\left(1 - R\right)^2}{2R}. \tag{2.23}$$

Now consider the q^{th} order resonance cavity with

$$\varphi_q = 2\pi q. \tag{2.24}$$

In the case that φ is close to φ_q, taking the second order Taylor expansion, $\cos\varphi$ can be written as

$$\cos\varphi \approx 1 - \frac{\left(\varphi - \varphi_q\right)^2}{2}. \tag{2.25}$$

Substituting this into Eq. (2.23), we get

$$\varphi - \varphi_q = \frac{1 - R}{\sqrt{R}}. \tag{2.26}$$

Then the full width at half maximum (FWHM) of the resonance is

$$\delta\varphi = \frac{2\left(1 - R\right)}{\sqrt{R}}. \tag{2.27}$$

In addition, the FWHMs expressed in terms of the frequency and cavity length can also be calculated:

$$\delta\nu = \frac{\mathrm{c}}{4\pi nl}\delta\varphi = \frac{\mathrm{c}}{2nl} \cdot \frac{1 - R}{\pi\sqrt{R}}, \tag{2.28}$$

$$\delta l = \frac{\mathrm{c}}{4\pi n\nu}\delta\varphi = \frac{\mathrm{c}}{2n\nu} \cdot \frac{1 - R}{\pi\sqrt{R}}. \tag{2.29}$$

To describe the relative sharpness of the resonance, the finesse $\mathcal{F}$ is defined as the ratio between the FWHM and FSR:

$$\mathcal{F} \equiv \frac{\Delta\varphi}{\delta\varphi} = \frac{\Delta\nu}{\delta\nu} = \frac{\Delta l}{\delta l} = \frac{\pi\sqrt{R}}{1-R}, \tag{2.30}$$

where $\Delta\varphi$ and Δl are the distances between neighbouring resonances expressed in phase and cavity length, respectively.

With the definition of finesse, Eq. (2.5) can be further simplified to

$$T_\mathrm{c} = \frac{T_1 T_2 \left(\frac{\mathcal{F}}{\pi}\right)^2}{1 + \left(\frac{2\mathcal{F}}{\pi}\right)^2 \sin^2\frac{\varphi}{2}}. \tag{2.31}$$

With this, the cavity resonance spectra are plotted in Fig. 2.6 with respect to the phase for different finesses. A higher finesse means sharper peaks in the resonance spectrum. To measure the finesse of a cavity, the easiest way is to measure the resonance spectrum, by varying either the frequency or the cavity length.

Under the approximation $\sin^2\frac{\varphi}{2} \approx \left(\frac{\varphi}{2}\right)^2$, it follows that the cavity resonance has a Lorentzian line shape. In general, a normalized Lorentzian line shape is

$$T(x) = \frac{1}{\pi}\frac{\delta/2}{(\delta/2)^2 + (x - x_0)}, \tag{2.32}$$

where x could be either φ, ν or l, and δ and x_0 are the corresponding FWHM and resonance value, respectively.

2.2.4 Transverse Modes

So far, only the longitudinal modes have been discussed. However, to describe the mode shape in three dimensions, transverse modes also have to be considered. In a geometry with cylindrical symmetry, the fundamental mode is a Gaussian mode, in particular the TEM$_{00}$ mode, which is a solution of Maxwell equations under paraxial approximation. Mathematically, for a given wavenumber k and wavelength λ, the Gaussian mode in free space has an electric field distribution as follows:

$$E(r,z) = E_0 \frac{w_0}{w(z)} \exp\left(-\frac{r^2}{w^2(z)} - i\frac{kr^2}{2R(z)} - ikz + \arctan\frac{z}{z_0}\right). \tag{2.33}$$

z is the coordinate along the optical axis and r is the transversal distance from the axis. w_0 is the smallest beam radius which is called beam waist. Then the Rayleigh range can be defined as follows:

$$z_0 = \frac{\pi w_0^2}{\lambda}. \tag{2.34}$$

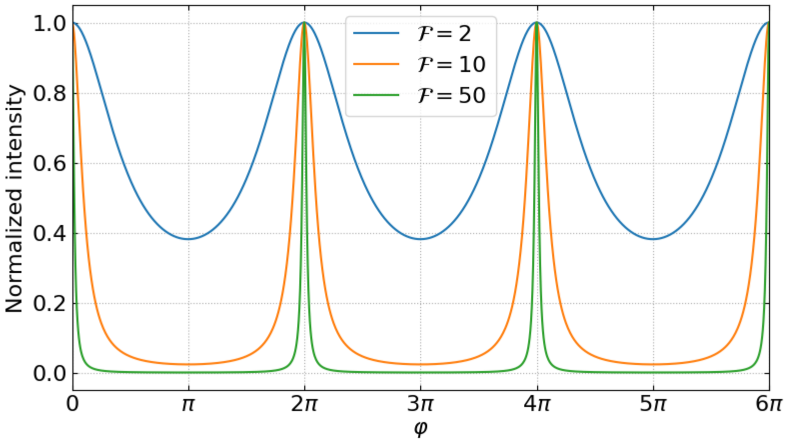

Figure 2.6: **Cavity resonance spectra for different finesses.** The intensity in the cavity is normalized to the maximum for each spectrum.

$w(z)$ is the beam radius at different longitudinal positions given by

$$w(z) = w_0 \sqrt{1 + \left(\frac{z}{z_0}\right)^2}. \tag{2.35}$$

$R(z)$ is the radius of curvature of the wavefront given by

$$R(z) = z \left(1 + \left(\frac{z_0}{z}\right)^2\right). \tag{2.36}$$

E_0 is the amplitude at the origin (focus). The prefactor $\frac{w_0}{w(z)}$ describes longitudinal mode profile and the first term of the exponent describes the transverse mode profile.

The intensity distribution of the Gaussian mode in Eq. (2.33) can then be easily calculated:

$$I(r, z) = I_0 \frac{w_0^2}{w^2(z)} \exp\left(-\frac{2r^2}{w^2(z)}\right), \tag{2.37}$$

where I_0 is the intensity at the origin. Such an intensity distribution is shown in Fig. 2.7.

In the cavity, a standing wave is formed with two counter-propagating Gaussian beams. By changing the sign of k in Eq. (2.33), the wave propagate in the $-z$ direction is obtained. Then the intensity distribution of a Gaussian mode in cavity becomes

$$I_c(r, z) = 2I_0 \frac{w_0^2}{w^2(z)} \exp\left(-\frac{2r^2}{w^2(z)}\right) \cos\left(kz + \frac{kr^2}{2R(z)}\right), \tag{2.38}$$

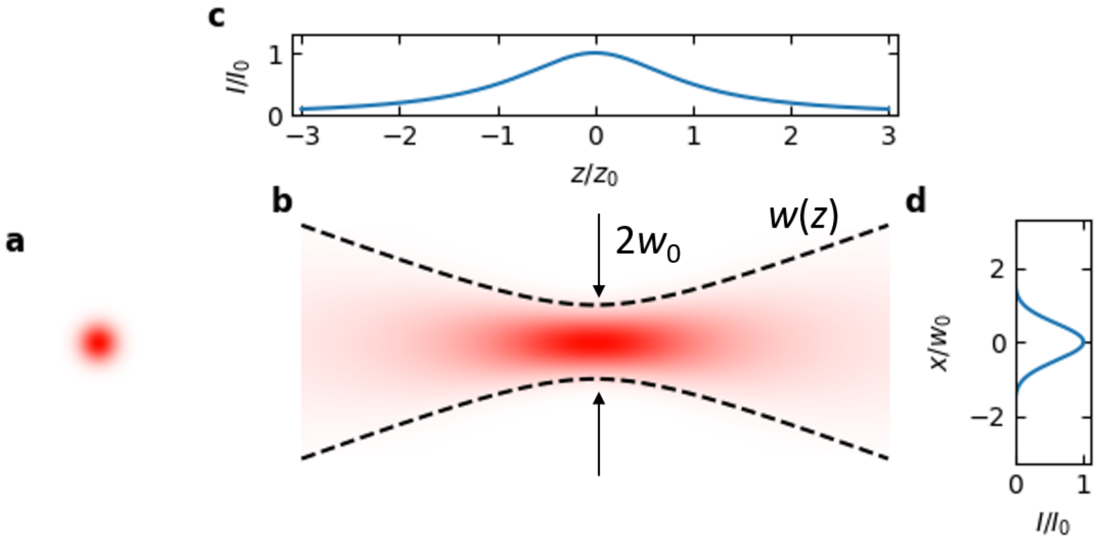

Figure 2.7: **Intensity distribution of a Gaussian mode in free space. a** and **b** are the beam profile in transverse and longitudinal plane, respectively. The dashed line in **b** shows the beam radius $w(z)$. The intensity distributions on longitudinal and transverse axis are shown in **c** and **d**, respectively.

which is shown in Fig. 2.8.

Besides the fundamental Gaussian mode, there are also higher-order transverse modes. They can be decomposed into different sets of eigen-modes, depending on which coordinate system is used.

Hermite-Gaussian modes are a set of eigen-modes in Cartesian coordinates, composed of Hermite polynomials $H_n(x)$:

$$\begin{aligned} E_{l,m}(x,y,z) &= E_0 \frac{w_0}{w(z)} H_l\left(\frac{\sqrt{2}x}{w(z)}\right) H_m\left(\frac{\sqrt{2}y}{w(z)}\right) \\ &\times \exp\left(-\frac{x^2+y^2}{w^2(z)} - i\frac{k\left(x^2+y^2\right)}{2R(z)} - ikz + (l+m+1)\arctan\frac{z}{z_0}\right), \end{aligned} \tag{2.39}$$

where l and m are mode orders referring to x and y direction, respectively. The shapes of some Hermite-Gaussian modes are shown in Fig. 2.9.

In cylindrical and elliptic coordinates, the transverse modes can be decomposed into Laguerre-Gaussian modes[46] and Ince-Gaussian modes,[47] respectively.

Unlike electrons, photons, as bosons, tend to occupy the state with the lowest energy. Therefore, the fundamental mode is usually dominant. However, when the

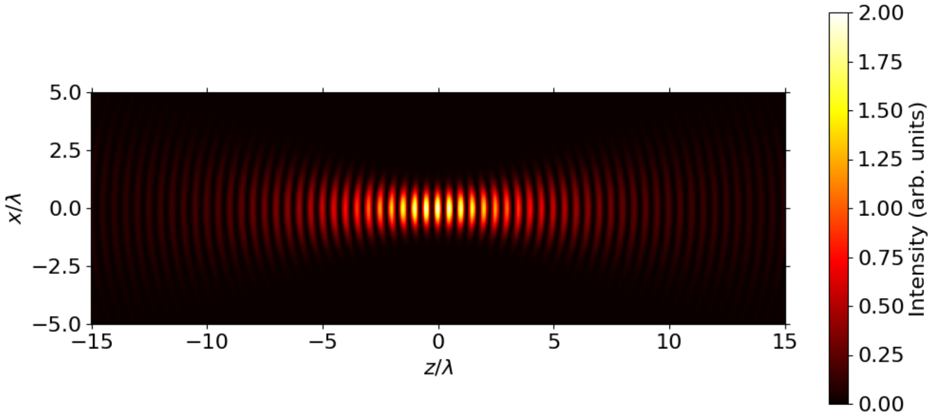

Figure 2.8: **Intensity distribution of a Gaussian mode in a cavity.** The beam waist z_0 is equal to the wavelength λ.

cylindrical symmetry is broken, higher-order modes could have comparable or even lower energies relative to the fundamental mode. In this case, higher-order modes can be observed.

By introducing an Au nanoparticle into a scannable microcavity, the point spread function of each transverse mode can be measured individually.[26] The cavity resonance spectrum and the mode shape of each transverse mode are shown in Fig. 2.10

Without birefringence, the cavity is isotropic to polarization. However, when a birefringent material is introduced into the cavity, separated polarization modes start to emerge.

For cavity enhanced spectroscopy, higher order modes and polarization modes are not favourable, because they lower the coupling into the fundamental mode. To eliminate these modes, the cavity has to be well aligned to keep cylindrical symmetry and the polarization of the laser has to be adjusted to match the birefringence of the cavity.

2.2.5 Losses in the Cavity

The finesse in Eq. (2.30), and thus the resonance spectra in Fig. 2.6, are only for lossless cavities. For a cavity with round trip loss L, a factor of $\sqrt{1-L}$ has to be multiplied to the mean reflectance R. The finesse then becomes

$$\mathcal{F} = \frac{\pi\sqrt{R\sqrt{1-L}}}{1-R\sqrt{1-L}}. \tag{2.40}$$

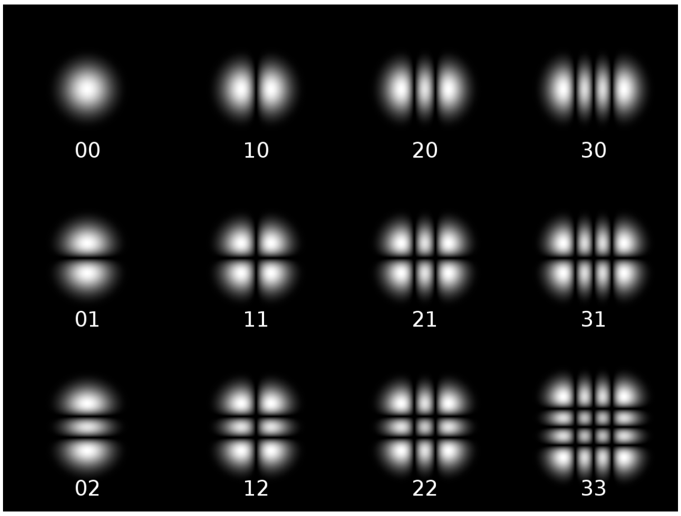

Figure 2.9: **Shapes of Hermite-Gaussian modes in the transverse plane.** The first and second number refers to l and m, respectively. The figure is taken from Ref. [45].

This relation can be used to calculate the losses introduced by the sample.

The cavity loss could come from interface scattering, media scattering and absorption.

Scattering at the interface can be described as diffuse reflectance as follows[48]

$$R_\mathrm{d} = R_0 \left(\frac{4\pi\sigma}{\lambda} \right)^2, \tag{2.41}$$

where R_0 is the specular reflectance and σ is the root mean square (RMS) roughness of the surface.

Media scattering can be classified into either Rayleigh scattering, Mie scattering or optical scattering depending on the relative size of the particles compared to the wavelength. In a bulk material, there is no significant media scattering.

The absorption of the sample in the cavity is determined by the spectral properties. By calculating the absorption from the measured finesse, the absorption spectroscopy in the cavity features a higher sensitivity.

All kinds of losses in the cavity will decrease the finesse and thus broaden the resonance peaks.

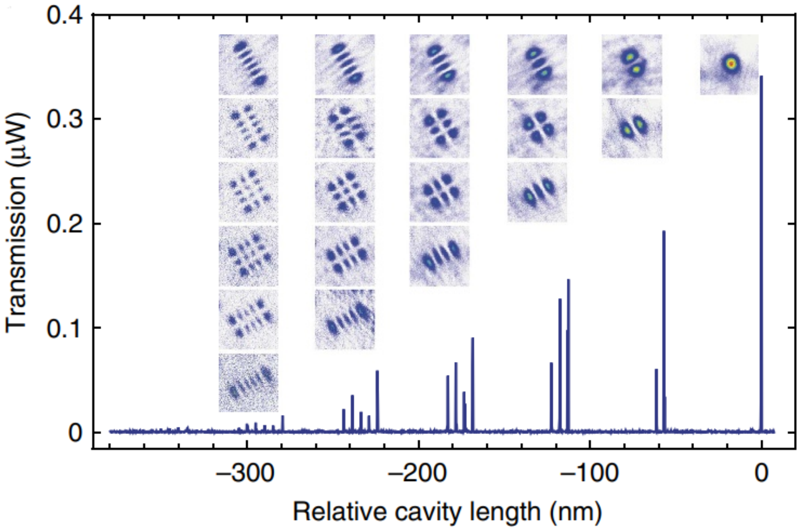

Figure 2.10: **Cavity transmission signal while tuning the cavity length.** The insets show the shapes of different transverse modes by scanning the cavity across an Au nanoparticle and evaluating the resonant transmission for each mode. The figure is taken from Ref. [26].

2.2.6 Mode Dispersion and Hybridization

In general, dispersion means the relation of a mode in the time domain and the spatial domain. In the case of a cavity, it is the relation between the frequency and the cavity length of a specific mode. Eq. (2.16) is the dispersion relation of the longitudinal modes in an empty cavity.

To visualize the mode dispersion, the cavity transmittance in Eq. (2.5) is calculated for different wavelengths and cavity lengths, as shown in Fig. 2.11. The cavity mode dispersion can be measured experimentally by scanning the frequency and cavity length simultaneously.

When a sample is mounted into the cavity, it becomes a hybrid cavity with two different media, an air gap with thickness l_a and a dielectric material with thickness l_d. Considering only the air gap, we get the pure air modes, which have the same dispersion relationship as the modes in an empty cavity. Considering only the dielectric material, we get the pure dielectric modes, which are independent of l_a. In a hybrid cavity, The electric fields in the two media are coupled to each other and have to fulfill the boundary conditions at the interface. Thus the air modes and dielectric modes are also coupled to each other, resulting in the hybridized modes.

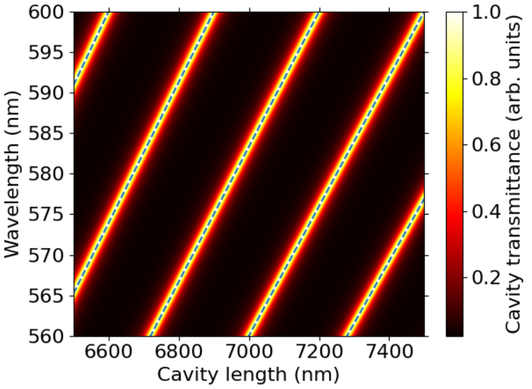

Figure 2.11: **Cavity mode dispersion of an empty cavity.** The finesse is set to be 10. The dashed lines from left to right show the longitudinal modes calculated with Eq. (2.16) from the 22th order to the 26th order, respectively.

The resonance condition of a hybrid cavity for a fixed l_d is given as follows:[49]

$$l_{\mathrm{a},q} = \frac{\lambda}{2\pi} \arctan\left(-\frac{1}{n_\mathrm{d}} \tan\left(\frac{2\pi n_\mathrm{d} l_\mathrm{d}}{\lambda_0}\right)\right) + \frac{q\lambda}{2}, \tag{2.42}$$

where n_d is the refractive index of the dielectric material and q is the mode order. Due to the boundary conditions, it is not possible to have a cavity resonant both in dielectric material and air gap at the same time, so an anti-crossing behavior will be observed.[50, 51] When the cavity is resonant in the air gap, the mode is called “air-like”, because such a mode behaves like a pure air mode. When the cavity is resonant in the dielectric material, the mode is called “dielectric-like”, because such a mode behaves like a pure dielectric mode. The dispersion of hybridized modes is shown in Fig. 2.12. A hybridized mode changes periodically between air-like and dielectric-like due to anti-crossings.

To further understand the mode hybridization, we simulate the mode dispersion using the matrix method described in Ref. [52]. We use two coated mirrors with design transmittances of 26% and 3%, called the low reflectivity (LR) mirror and the high reflectivity (HR) mirror respectively. The thickness of the crystal is set to be 5 μm and the refractive index of the crystal is set to be 1.5. The parameters are chosen as such as they are similar to those values we use in the experiment, which will be discussed in chapter 3.

The results of the simulation are shown in Fig. 2.13a and b, with the crystal lying on the LR mirror and the HR mirror, respectively. When the crystal lies on the LR mirror, the dielectric-like modes have lower transmission, and vice versa. This can be explained by comparing the finesses of the air-cavity and the dielectric-cavity.

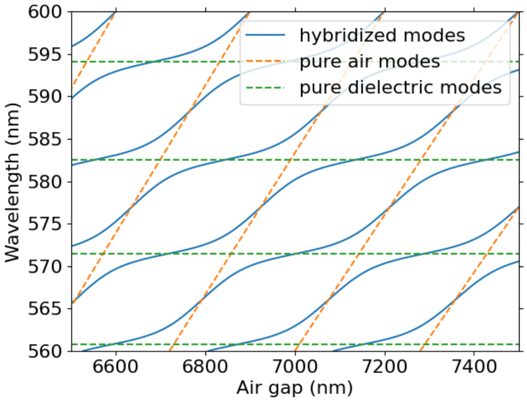

Figure 2.12: **Hybridized cavity modes in comparison with pure air modes and dielectric modes.** The pure air modes are the same as in Fig. 2.11. The pure dielectric modes are calculated with $\lambda_q = 4n_\mathrm{d}l_\mathrm{d}/(2q-1)$.[49] A hybridized mode becomes air-like when it intersects with a pure air mode and becomes dielectric-like when it intersects with a pure dielectric mode.

In a hybrid cavity, there are three reflective surfaces: the mirror, the fiber end facet and the interface between the dielectric material and the air gap. Thus, two cavities are formed. We call the one that arises in the air gap an air-cavity and the other one that arises in the dielectric material a dielectric-cavity. The mode hybridization arises from the coupling between these two cavities. If the air-cavity has a higher finesse, then the hybrid cavity features a higher transmission for the air-like modes, which is the case in Fig. 2.13a. The same accounts for the case of a dielectric-cavity, which is shown in Fig. 2.13b.

To show the difference between air-like and dielectric-like modes, we simulate the electric field intensity distribution of those two modes. Fig. 2.13c shows the air-like mode highlighted by a blue circle in Fig. 2.13b and Fig. 2.13d shows the dielectric-like mode highlighted by a red circle in Fig. 2.13b. As indicated by the names, the energy of an air-like mode is mostly distributed within the air-cavity and the energy of a dielectric-like mode is mostly within the dielectric-cavity. For the dielectric-like case, shown in Fig. 2.13d, the electric field intensity is not higher within the dielectric-cavity, but the energy density, which is proportional to $n^2|E|^2$, is higher than that within the air-cavity. In addition, at the interface between air gap and the dielectric material, the air-like mode exhibits a node while the dielectric-like mode shows an anti-node.

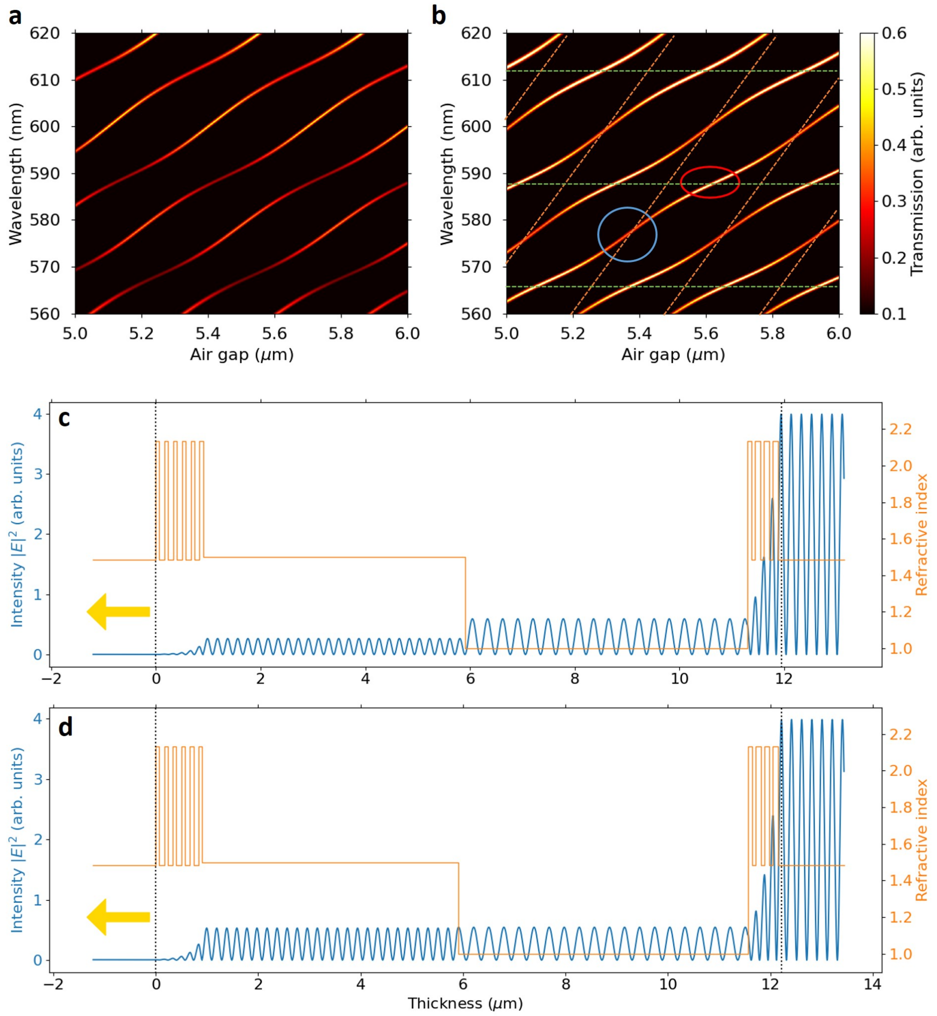

Figure 2.13: **Simulated mode dispersion.** The transmission of air-like and dielectric-like modes are compared for the crystal lying on the LR mirror and the HR mirror. **a**: Mode dispersion of a hybrid cavity with the crystal lying on the LR mirror. In this case, the air-like modes have higher transmission. **b**: Mode dispersion of a hybrid cavity with the crystal lying on the HR mirror. In this case, the dielectric-like modes have higher transmission. The pure air modes, orange lines, and pure dielectric modes, green lines, are reconstructed by connecting air-like and dielectric-like modes, respectively. As examples, the electric field distribution of the air-like mode highlighted by the blue circle and the dielectric-like mode highlighted by the red circle are shown in **c** and **d**, respectively. **c**: Simulated electric field distribution of an air-like mode. The light propagates from right to left. **d**: Simulated electric field distribution of an dielectric-like mode. The light propagates from right to left.

2.2.7 Characteristics of the Cavity

There are several parameters required to fully characterize a cavity. Depending on the applications, some are more important than the others.

As defined in Eq. (2.30), the finesse describes the sharpness of the resonance peaks, which represents the spectral confinement of the cavity. When the cavity resonance is tuned precisely to the emission line of the emitters in the cavity, the emission will be significantly enhanced. This is called Purcell enhancement, which will be discussed in detail in Sec. 2.3. Using the resonance linewidth in Eq. (2.28), the cavity photon lifetime can be calculated as

$$\tau = \frac{1}{2\pi\delta\nu} = \frac{\mathcal{F}}{2\pi\Delta\nu}, \tag{2.43}$$

then the average number of round trips before a photon leaves the cavity is

$$N = \tau\Delta\nu = \frac{\mathcal{F}}{2\pi}. \tag{2.44}$$

This shows, that from another perspective, the finesse indicates how long a cavity can trap the photons.

The quality factor, or Q-factor, describes how underdamped a resonator is. It is the ratio between the resonance frequency and the resonance linewidth:

$$Q = \frac{\nu}{\delta\nu} = q\mathcal{F}. \tag{2.45}$$

Similar to finesse, quality factor also describes the sharpness of the resonance peaks, but relative to the frequency.

The mode volume is the volume that a cavity mode occupies. In general, it is defined as

$$V_\mathrm{m} \equiv \frac{1}{E_0^2} \iiint\limits_V |E(\mathbf{r})|^2 \mathrm{d}V, \tag{2.46}$$

where $E(\mathbf{r})$ is the electric field amplitude at location $\mathbf{r}$ and E_0 is the maximum electric field amplitude. For a fundamental Gaussian mode, the mode volume is given by

$$V_\mathrm{m} = \frac{\pi w_0^2 l}{4}. \tag{2.47}$$

The mode volume describes the spatial confinement of the cavity.

In application, it is always the combination of spectral and spatial confinement that determines the performance of the cavity. Table 2.2 lists some figures of merit (FOM) for different applications.[53]

Application	Regime	FOM
Purcell effect	Bad cavity	Q/V_m
	Bad emitter	$1/V_\mathrm{m}$
Strong coupling with two level emitter	Bad cavity	$Q/\sqrt{V_\mathrm{m}}$
	Bad emitter	$1/\sqrt{V_\mathrm{m}}$

Table 2.2: **Figures of merit for different applications with cavity.** Bad cavity means the cavity has a broader linewidth while bad emitter means the emitter has a broader linewidth.

2.2.8 Fiber-based microcavity

To increase the spatial confinement of the photons, a fiber-based microcavity composed of a single mode fiber and a planar mirror was designed.[26] According to Eq. (2.15), in order to form a stable cavity in this configuration, the cavity length has to be smaller than the radius of curvature of the fiber end facet. To increase the finesse, a reflective coating is used on both the mirror and the fiber end facet. In Ref. [26], the finesse reaches 57,000.

2.3 Purcell Enhancement

To describe the confinement implemented by the cavity, a theoretical model is needed. In a quantum picture of light-matter interaction, the atomic states are strongly coupled with the photonic states. This coupling is significantly enhanced when some specific conditions are fulfilled. This is called Purcell enhancement, or the Purcell effect.[54] Purcell enhancement is observed as a higher spontaneous emission rate.

2.3.1 Models for Light-matter Interaction

To differentiate the quantum model from the classical model and the semi-classical model, we will first introduce the other two models briefly.

The classical model is based on classical mechanics and electrodynamics, where the matter is treated as an ensemble of charged particles governed by Newton's equations and the light is treated as an electromagnetic field governed by Maxwell's equations. With the classical model, linear and nonlinear optical phenomena can be explained.

In the semi-classical model, the atomic system is quantized, while the light is still treated as a classical electromagnetic field, which acts as a time-dependent Hamiltonian. The evolution of the atomic system can be derived using the time-dependent

Schrödinger equation (TDSE). With the semi-classical model, Rabi oscillations can be explained, but not spontaneous emission.

In the quantum model, the electromagnetic field is also quantized. Rather than the field, the concept of photonic states is adopted. The states of the system are described by a combination of atomic and photonics states. An atomic excitation can be converted into a photon and vice versa.

2.3.2 Quantization of the Electromagnetic Field

Considering an 1D-optical cavity with length l in the z-direction, the electric field and magnetic field are polarized in x- and y-directions, respectively. A general solution to the Maxwell's equations can be written as

$$\begin{aligned} E_x(z,t) &= \sum_j A_j q_j(t) \sin\left(k_j z\right), \\ H_y(z,t) &= \sum_j A_j \left(\frac{\dot{q}_j(t)\varepsilon_0}{k_j}\right) \cos\left(k_j z\right), \end{aligned} \tag{2.48}$$

where $q_j(t)$ is the normal mode amplitude with units of length, $k_j = j\pi/l$ and

$$A_j = \sqrt{\frac{2\omega_j^2 m_j}{V_m \varepsilon_0}}, \tag{2.49}$$

with $\omega_j = j\pi c/l$ as the eigenfrequency of the cavity and V_m as the mode volume, which is defined in Eq. (2.47). m_j is a constant with units of mass.

The classical Hamiltonian of such a dynamic system is then

$$\begin{aligned} H &= \frac{1}{2}\int_V \mathrm{d}\tau \left(\varepsilon_0 E_x^2 + \mu_0 H_y^2\right) \\ &= \frac{1}{2}\sum_j \left(m_j \omega_j^2 q_j^2 + m_j \dot{q}_j^2\right) \\ &= \frac{1}{2}\sum_j \left(m_j \omega_j^2 q_j^2 + \frac{p_j^2}{m_j}\right), \end{aligned} \tag{2.50}$$

where $p_j = m_j \dot{q}_j$ is the canonical momentum. The Hamiltonian has the same expression as a harmonic oscillator.

By quantization, q_j and p_j become operators $\hat{q}_j$ and $\hat{q}_j$, for which the following commutation relations apply:

$$[\hat{q}_i, \hat{p}_j] = i\hbar\delta_{ij}, \tag{2.51}$$

$$[\hat{q}_i, \hat{q}_j] = [\hat{p}_i, \hat{p}_j] = 0. \tag{2.52}$$

Through a canonical transformation, the annihilation and the creation operators can be derived as follows:

$$\hat{a}_j = \frac{1}{\sqrt{2m_j\hbar\omega_j}}\left(m_j\omega_j\hat{q}_j + i\hat{p}_j\right), \tag{2.53}$$

$$\hat{a}_j^\dagger = \frac{1}{\sqrt{2m_j\hbar\omega_j}}\left(m_j\omega_j\hat{q}_j - i\hat{p}_j\right), \tag{2.54}$$

together with the commutation relations

$$[\hat{a}_i, \hat{a}_j^\dagger] = i\hbar\delta_{ij}, \tag{2.55}$$

$$[\hat{a}_i, \hat{a}_j] = [\hat{a}_i^\dagger, \hat{a}_j^\dagger] = 0. \tag{2.56}$$

The Hamiltonian becomes

$$\hat{H} = \hbar\sum_j \omega_j \left(\hat{a}_i^\dagger\hat{a}_j + \frac{1}{2}\right). \tag{2.57}$$

The quantized electric field operator is

$$\hat{E}_x(z) = \sum_j E_{0,j}\left(\hat{a}_j + \hat{a}_j^\dagger\right)\sin\left(k_j z\right), \tag{2.58}$$

with

$$E_{0,j} = \sqrt{\frac{\hbar\omega_j}{V_m\varepsilon_0}}. \tag{2.59}$$

In the case of free space, Eq. (2.58) becomes

$$\hat{\mathbf{E}}(\mathbf{r}) = \sum_{\mathbf{k}} \mathbf{E}_{0,\mathbf{k}}\left(\hat{a}_{\mathbf{k}}\mathrm{e}^{i\mathbf{k}\cdot\mathbf{r}} + \hat{a}_{\mathbf{k}}^\dagger\mathrm{e}^{-i\mathbf{k}\cdot\mathbf{r}}\right), \tag{2.60}$$

with

$$\mathbf{E}_{0,\mathbf{k}} = \mathbf{e}_{\mathbf{k}}\sqrt{\frac{\hbar\omega_{\mathbf{k}}}{2V_m\varepsilon_0}}, \tag{2.61}$$

where $\mathbf{e}_{\mathbf{k}}$ is the unit polarization vector.

For a specific mode, the eigenstates of the Hamiltonian are called Fock states $|n\rangle$, and has the following properties:

$$\hat{H}\,|n\rangle = E_n\,|n\rangle = \hbar\omega\left(n + \frac{1}{2}\right), \tag{2.62}$$

$$\hat{a}_i^\dagger\,|n\rangle = \sqrt{n+1}\,|n+1\rangle, \tag{2.63}$$

$$\hat{a}_i\,|n\rangle = \sqrt{n}\,|n-1\rangle, \tag{2.64}$$

$$|n\rangle = \frac{\left(\hat{a}_i^\dagger\right)^n}{\sqrt{n!}}\,|0\rangle. \tag{2.65}$$

These states are also called number states, because n is the number of photons.

2.3.3 Spontaneous Emission in a Fully Quantum Model

Spontaneous emission arises from the coupling between an atomic system and vacuum fluctuations. In order to describe such a phenomenon, a quantized field is required a fully quantized Hamiltonian can be written as

$$\hat{H} = \hat{H}_\mathrm{A} + \hat{H}_\mathrm{F} + \hat{H}_\mathrm{I}, \tag{2.66}$$

with the three components representing the atomic system, the electromagnetic field and the interaction between them, respectively.

For a two-level atomic system, the atomic states are denoted as $|g\rangle$ and $|e\rangle$ for ground state and excited state, respectively. In general, a photonic state can be written as

$$|\psi_\mathrm{ph}\rangle = \prod_{\mathbf{k}}^{\otimes} |n_\mathbf{k}\rangle\,, \tag{2.67}$$

where $\mathbf{k}$ denotes a mode in free space. The photonic ground state can be written as

$$|0, \cdots, 0_\mathbf{k}, \cdots, 0\rangle \equiv |0\rangle\,, \tag{2.68}$$

where each mode is in the ground state. The single-excitation of the photonic state in mode k can be written as

$$|0, \cdots, 1_\mathbf{k}, \cdots, 0\rangle \equiv |\mathbf{k}\rangle\,, \tag{2.69}$$

where only the mode $\mathbf{k}$ is excited and all other modes are in the ground state. Spontaneous emission corresponds to the transition from $|e, 0\rangle$ to $|g, \mathbf{k}\rangle$. In the case of a weak perturbation, the spontaneous emission rate can be calculated with Fermi's golden rule:

$$\Gamma = \frac{2\pi}{\hbar^2} \sum_{\mathbf{k}} \left| \langle g, \mathbf{k}|\, \hat{H}_\mathrm{I} \,|e, 0\rangle \right|^2 \delta\left(\omega_0 - \omega_\mathbf{k}\right)\,, \tag{2.70}$$

where ω_0 is the resonance frequency of the atomic system. The dipole interaction between the electric field and the atomic system is given by

$$\hat{H}_\mathrm{I} = -\mathrm{e}\hat{\mathbf{E}} \cdot \hat{\mathbf{r}}. \tag{2.71}$$

The transition matrix element can then be simplified as follows:

$$\begin{aligned} \left| \langle g, \mathbf{k}|\, \hat{H}_\mathrm{I} \,|e, 0\rangle \right|^2 =& \left| -\mathrm{e} \,\langle g, \mathbf{k}|\, \hat{\mathbf{E}} \cdot \hat{\mathbf{r}} \,|e, 0\rangle \right|^2 \\ =& \left| \boldsymbol{\mu}_{eg} \cdot \mathbf{E}_{0,\mathbf{k}} \,\langle \mathbf{k}|\, \hat{a}_\mathbf{k} \mathrm{e}^{i\mathbf{k}\cdot\mathbf{r}} + \hat{a}_\mathbf{k}^\dagger \mathrm{e}^{-i\mathbf{k}\cdot\mathbf{r}} \,|0\rangle \right|^2 \\ =& \left| \boldsymbol{\mu}_{eg} \cdot \mathbf{E}_{0,\mathbf{k}} \right|^2, \end{aligned} \tag{2.72}$$

where $\mu_{eg} \equiv -\mathrm{e} \langle g| \hat{\mathbf{r}} |e\rangle$ is the dipole moment of the atomic system. In the second step, we use Eq. (2.60) to substitute $\hat{\mathbf{E}}$. Then the spontaneous emission rate in Eq. (2.70) becomes

$$\Gamma = \frac{2\pi}{\hbar^2}\frac{1}{3}\mu_{eg}^2 \frac{\hbar\omega_0}{2V_m\varepsilon_0}\rho\left(\omega_0\right) = \frac{\pi\omega_0}{3\hbar V_m\varepsilon_0}\mu_{eg}^2\rho\left(\omega_0\right). \tag{2.73}$$

The factor of 1/3 arises from the different dipole orientations and $\rho\left(\omega_0\right)$ is the density of states of photons in a mode volume of V_m, which is

$$\rho\left(\omega_0\right) = \frac{V_m n^3 \omega_0^2}{\pi^2 \mathrm{c}^3} \tag{2.74}$$

for free space. We therefore arrive at the spontaneous emission rate in free space

$$\Gamma_0 = \frac{\mu_{eg}^2 n^3 \omega_0^3}{3\pi\varepsilon_0\hbar \mathrm{c}^3}. \tag{2.75}$$

2.3.4 Cavity Enhancement and Purcell Factor

In an optical cavity, we consider the spontaneous emission coupled into a specific cavity mode with resonance frequency ω_0 and field strength

$$\mathbf{E}_{0,\mathrm{c}} = \mathbf{e}_{\mathrm{c}}\sqrt{\frac{\hbar\omega_0}{2V_m\varepsilon_0}}u(\mathbf{r}), \tag{2.76}$$

where $u(\mathbf{r})$ describes the mode profile. Eq. (2.70) becomes

$$\begin{aligned}\Gamma =& \frac{2\pi}{\hbar^2}\left|\langle g,\mathrm{c}| \hat{H}_{\mathrm{I}} |e,0\rangle\right|^2 \rho_{\mathrm{c}}(\omega_0)\\ =& \frac{2\pi}{\hbar^2}\left|\boldsymbol{\mu}_{eg}\cdot\mathbf{E}_{0,\mathrm{c}}\right|^2\rho_{\mathrm{c}}(\omega_0).\end{aligned} \tag{2.77}$$

Here c stands for a specific cavity mode and the density of states follows the Lorentzian line shape:

$$\rho_{\mathrm{c}}(\omega) = \frac{1}{\pi}\frac{\delta\omega/2}{\left(\delta\omega/2\right)^2 + \left(\omega-\omega_0\right)^2} \tag{2.78}$$

and

$$\rho_{\mathrm{c}}(\omega_0) = \frac{2}{\pi\delta\omega} = \frac{2Q_{\mathrm{c}}}{\pi\omega_0}, \tag{2.79}$$

where Q_{c} is the quality factor of the cavity resonance. The maximum spontaneous emission rate into a cavity mode is then

$$\gamma_{\mathrm{c,max}} = \frac{2\pi}{\hbar^2}\mu_{eg}^2\frac{\hbar\omega_0}{2V_m\varepsilon_0}\frac{2Q}{\pi\omega_0} = \frac{2\mu_{eg}^2 Q_{\mathrm{c}}}{\hbar\varepsilon_0 V_{\mathrm{m}}}. \tag{2.80}$$

The Purcell factor can then be defined as

$$C \equiv \frac{\gamma_{\mathrm{c,max}}}{\gamma_0} = \frac{6\pi c^3}{n^3\omega_0^3}\frac{Q_{\mathrm{c}}}{V_{\mathrm{m}}} = \frac{3}{4\pi^2}\left(\frac{\lambda}{n}\right)^3\frac{Q_{\mathrm{c}}}{V_{\mathrm{m}}}, \tag{2.81}$$

where λ is the wavelength of the light in vacuum. Such an enhancement of the spontaneous emission rate is called the Purcell effect.

So far we have assumed that the atomic transition has an infinitely narrow linewidth, which is valid when the cavity resonance is much broader than the atomic transition, also called bad cavity regime in Tab. 2.2.

If the atomic transition has a finite linewidth, then the density of states becomes the integral of the emission line multiplied by the cavity line:

$$\rho\left(\omega_0\right) = \int_{-\infty}^{\infty}\rho_{\mathrm{c}}\left(\omega-\omega_0\right)S\left(\omega\right)\mathrm{d}\omega, \tag{2.82}$$

where $S(\omega)$ is the emission line of the atomic system. If the cavity line is symmetric, then this simplifies to the convolution of the cavity line and the emission line. Assuming that the emission line is also Lorentzian, with a quality factor Q_{em}, then the Q-factor of the convoluted line becomes:

$$Q_{\mathrm{eff}} = \frac{1}{Q_c^{-1}+Q_{\mathrm{em}}^{-1}}, \tag{2.83}$$

so the Purcell factor is

$$C = \frac{3}{4\pi^2}\left(\frac{\lambda}{n}\right)^3\frac{Q_{\mathrm{eff}}}{V_{\mathrm{m}}}. \tag{2.84}$$

If $Q_{\mathrm{em}} \ll Q_{\mathrm{c}}$, then $Q_{\mathrm{eff}} \approx Q_{\mathrm{em}}$, so the Purcell effect is mostly affected by the mode volume V_{m}. This regime is called bad emitter regime in table 2.2.

Chapter 3

Experimental Setup

In this chapter, we introduce our microcavity in detail and show how different measurements can be carried out in the cavity. Following this, we describe our crystallization method to integrate the molecular complexes to the microcavity.

3.1 Fiber-based Fabry-Pérot Scanning Microcavity

To make use of the cavity enhancement of an ensemble sample, we utilize a microcavity composed of a planar mirror[1] and a laser-machined single mode fiber[2] with a concave profile. The crystalline sample is grown on the mirror. Both the mirror and the fiber end facet are coated with dielectric materials to increase the reflectivity, and thus the finesse.

3.1.1 Fabrication of Cavity Fibers

A microcavity can be fabricated with low surface roughness, either by etching[25] or by laser-machining[22]. The etching method can fabricate structures in the range of 100 μm. However, with laser-machining, the scale of the profile can achieve features on the order of 10 μm.

We use a pulsed CO_2-laser[3] with a peak power >10 W and a tunable duty cycle. The high intensity of the laser will evaporate the material at the shot area. The heat conduction can be controlled by the duty cycle. Using an acousto-optic modulator (AOM), the pulse sequence can be freely designed with MHz bandwidth.

---

[1] Ø12.7 mm × 3.0 mm, out of SiO_2

[2] Artphotonics SM530-125-160AL

[3] Synrad firestar v40, $\lambda_{CO_2} = 10.6\ \mu$m

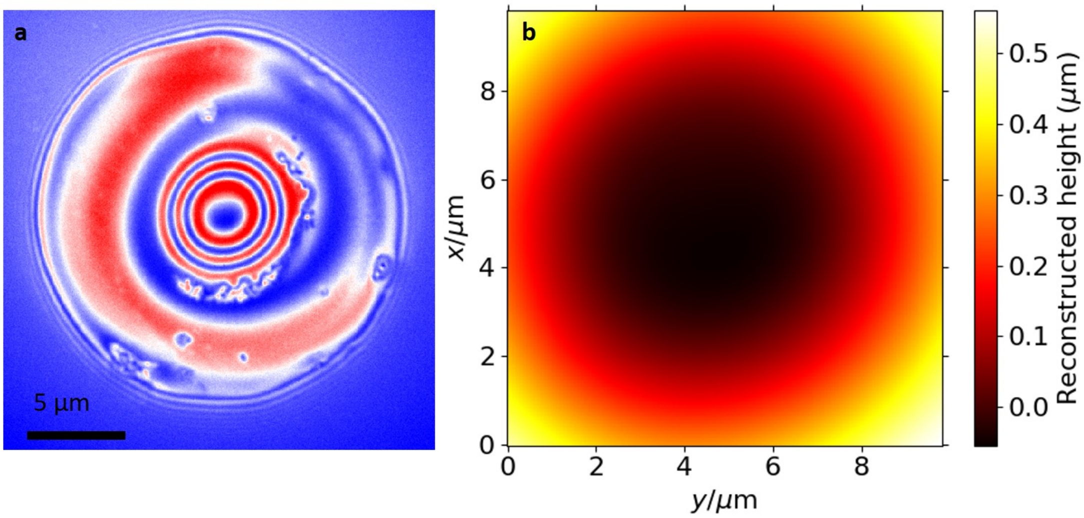

Figure 3.1: **Characterization of the fiber in the WLI. a**: The interference pattern captured by the camera. **b**: Reconstruction of the fiber end facet from the interference pattern. Only the center part is reconstructed. The fiber was shot by 5 pulses with a duration of 22 μs and 40 ms pause in between. The ROC in $x-$ and y-direction are 50.9 μm and 34.3 μm, respectively, given by a 2D Gaussian fit.

In order to characterize the fiber, a white light interferometer (WLI) is used. A light-emitting diode (LED) centered at 463.25 nm is used to illuminate the fiber and the interference pattern is captured by a camera, from which the phase information can be reconstructed into height profiles. The interference pattern and reconstructed profile of one of the fibers used in this study are shown in Fig. 3.1. From the reconstruction data, the radius of curvature (ROC) and the depth of the profile can be determined. According to Eq. (2.15), the ROC determines the stability range of the cavity.

3.1.2 Reflective Coating

The reflective coating is achieved by distributed Bragg reflectors (DBRs), applying on both the mirror and the fiber end facet. DBRs consist of a sequence of thin dielectric layers with alternating materials, arranged in such a way that the reflected wave from each interface will all interfere constructively. The reflectivity R of a DBR consist of two alternating materials with refractive indices $n_{\mathrm{H}} > n_{\mathrm{L}}$ can be

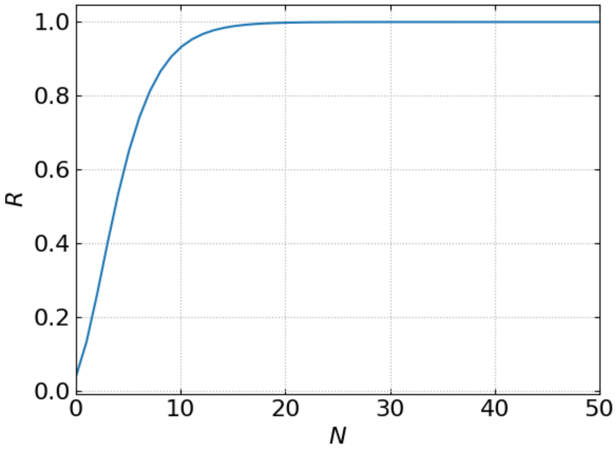

Figure 3.2: **Reflectivity of a DBR as a function of the number of stacks.**

approximated as[55]:

$$R = \left(\frac{n_0 n_\mathrm{L}^N - n_\mathrm{S} n_\mathrm{H}^N}{n_0 n_\mathrm{L}^N + n_\mathrm{S} n_\mathrm{H}^N} \right)^2 , \tag{3.1}$$

where n_0 is the refractive index of the medium in the cavity, n_S is the refractive index of the mirror substrate, and N is the number of stacks. We use Ta_2O_5 ($n = 2.1324$) and SiO_2 ($n = 1.4829$) as the coating materials. Taking $n_0 = 1$ and $n_\mathrm{S} = n_{\mathrm{SiO_2}} = 1.48$, we plot the reflectivity R in Eq. (3.1) with respect to N, as shown in Fig. 3.2.

A DBR coating is only designed for a specific wavelength, since different wavelengths will have different phases in the coating layers, thus the constructive interference is not guaranteed. Therefore each individual DBR coating can be simulated for different center wavelengths.

Using the matrix method described in Ref. [52], we simulate the transmittance for different multi-layer coating sequences, as shown in Fig. 3.3. The Sellmeier formula[56] is used to model the medium dispersion. The coating consists of alternating Ta_2O_5 and SiO_2 layers, starting with Ta_2O_5 from the mirror substrate. As shown in Fig. 3.3, DBRs feature a band of very low transmittance centered at the design wavelength, which is called stop band. The more layers, the lower the transmittance within the stop band and the steeper the edge of the stop band.

In this thesis, we use a single mode fiber coated[4] with 31 layers, resulting in a transmittance of 25 parts per million (ppm), and a planar mirror coated with 28 layers, resulting in a transmittance of 200 ppm, with a design wavelength of 585

---

[4] The coating is done by Laseroptik GmbH

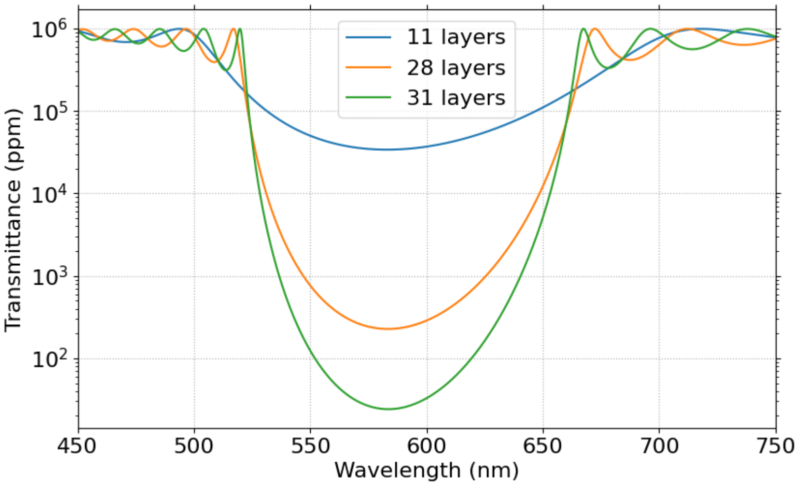

Figure 3.3: **Transmittance through DBRs with different coating layers. The design wavelength is 585 nm.** The transmittance is shown in ppm.

nm. According to Eq. (2.30), the design finesse is around 28,000.

3.1.3 Assembly of the Microcavity

The mechanical setup of the microcavity is shown from two different angles in Fig. 3.4 and 3.5. The design was introduced by Thomas Hümmer in his PhD thesis [57]. The particular setup used in this thesis was built by Evgenij Vasilenko.

The cavity fiber is fed through and glued[5] into a syringe needle[6] (2), which is then mounted into a cantilever (1). The longitudinal movement is controlled by a coarse[7] (6) and a fine[8] z-piezo (5), pressing on the cantilever. The lateral movement is controlled by a x-piezo[9] (3) pressing on the needle, and a y-piezo[10] (4) pressing on the cantilever. Rather than directly translating the fiber, the three piezos tilt the cantilever. Therefore, it is important to adjust the screws (9, 10, 11), such that the fiber is perpendicular to the mirror when the piezos are not charged. At room temperature, the cavity has a longitudinal scanning range of 30 μm and a lateral scanning range of 70 μm. Due to the different mechanical structures for x- and y-movement, the scanning range in the x-direction is larger than that in the

---

[5] Uhu plus schnellfest.

[6] Sterican Blunt, 27 G × 1", Ø0.40×25 mm.

[7] Piezomechanik PSt 150/5×5/20

[8] Thorlabs, PA4FEW

[9] Piezomechanik PSt 150/2×3/20

[10] Piezomechanik PSt 150/3.5×3.5/20

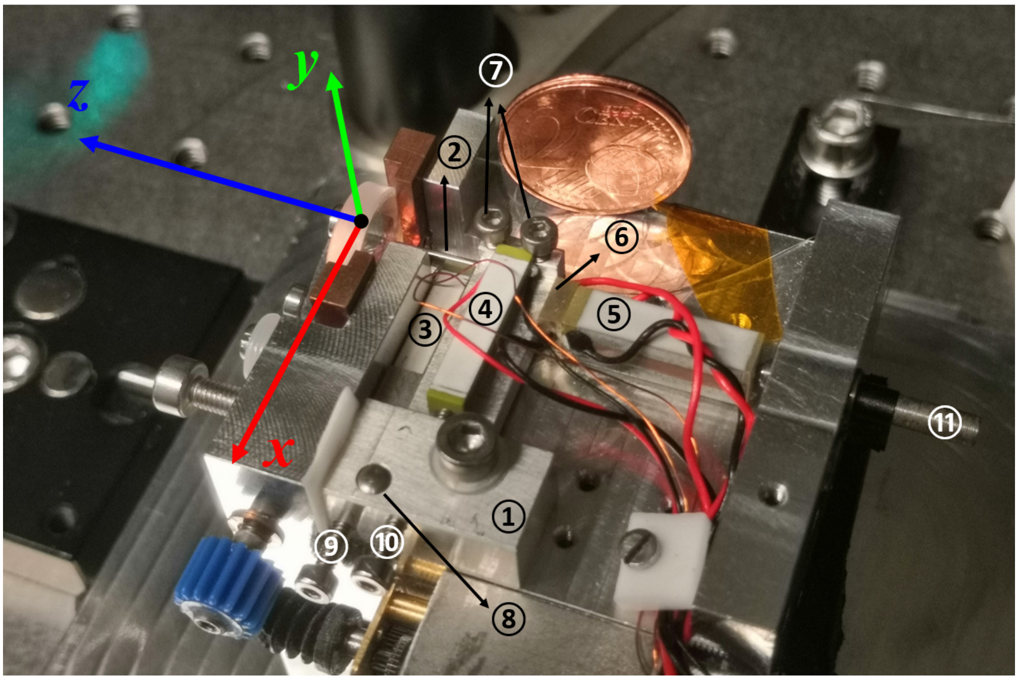

Figure 3.4: **Mechanical structure of the fiber positioning setup.** The labeled parts are explained as follows: ①: The cantilever, which looks like an inverted "T" in the figure. ②: The syringe needle mounted at the end of the cantilever, with the fiber glued inside. ③: x-piezo, pressing onto the needle. ④: y-piezo, pressing onto the end of the cantilever, which will twist the cantilever and thus move the fiber in y-direction. ⑤ and ⑥: Coarse and fine z-piezos, pressing onto the end of the cantilever. ⑦: Mounting screws for the needle. ⑧: The rotation axis of the cantilever. ⑨, ⑩ and ⑪: The adjusting screws for the x-, y- and z-piezos, respectively. The coin is used for scale.

y-direction.

The mirror is mounted on a translation stage driven by two motors. The travel range is sufficient to reach the central 5 mm region of the mirror. More details about the operation of the cavity will be discussed in Sec. 3.2.

A picture taken by a microscope[11] reveals more details about the microcavity, as shown in Fig. 3.6.

---

[11] Reflecta DigiMicroscope USB 200

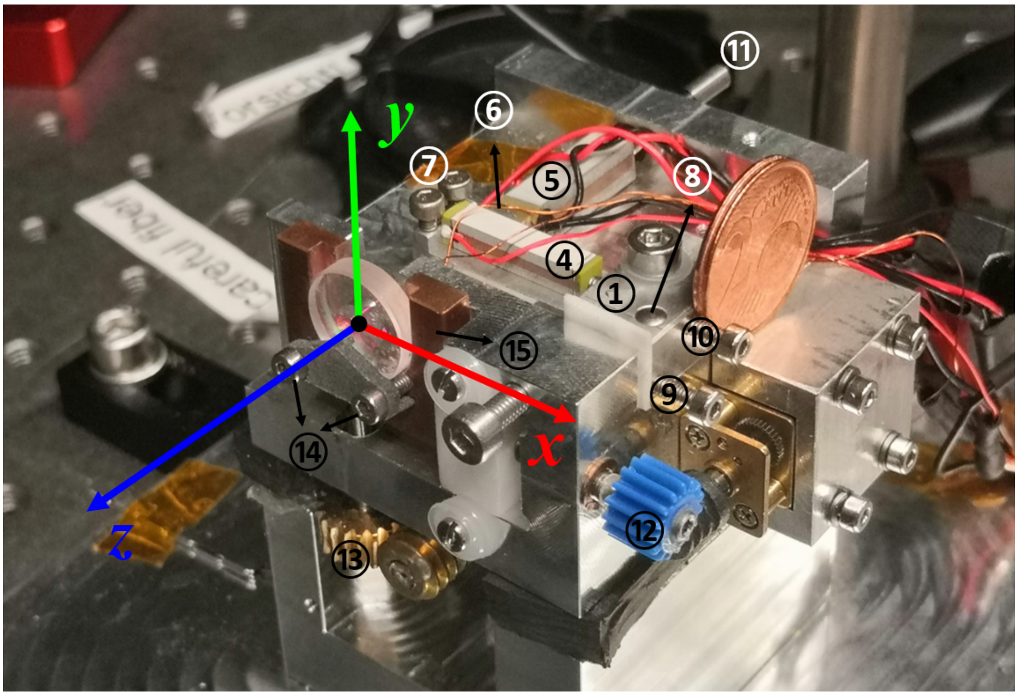

Figure 3.5: **Mechanical structure of the mirror translation stage.** The labeled parts are explained as follows: ⑫: The gear to move the mirror in x-direction. ⑬: The gear to move the mirror in y-direction. ⑭: Mounting screws for the mirror. ⑮: Mirror holder which can be moved in x- and y-direction. The coin is used for scale.

3.1.4 Optical Setup

The sketch of the optical setup is shown in Fig. 3.7. The laser is coupled into the cavity via the cavity fiber, which enables an easy exchange of the light sources. A diode laser[12] with center wavelength of 532 nm and tunable power up to 100 mW is used for off-resonant excitation, which drives the $^7F_0 \rightarrow {}^5D_1$, followed by phonon-assisted relaxation to $^5D_0$ and further via photon emission. A dye laser[13] with tunable wavelength around 580 nm is used for resonant excitation, which directly drive the $^7F_0 \rightarrow {}^5D_0$ transition. Therefore, the DBR coating is designed for this wavelength. A pulsed broadband laser[14] is used to measure the wavelength-dependent transmittance and mode dispersion. With a multi-channel tunable filter[15] based on acousto-optic tunable filter technology (AOTF), the broadband laser can be filtered to a single wavelength output with a bandwidth of about 2 nm.

---

[12] Cobolt Samba 100

[13] Sirah Matisse 2 DX

[14] SuperK fianium FIR-20

[15] SuperK select

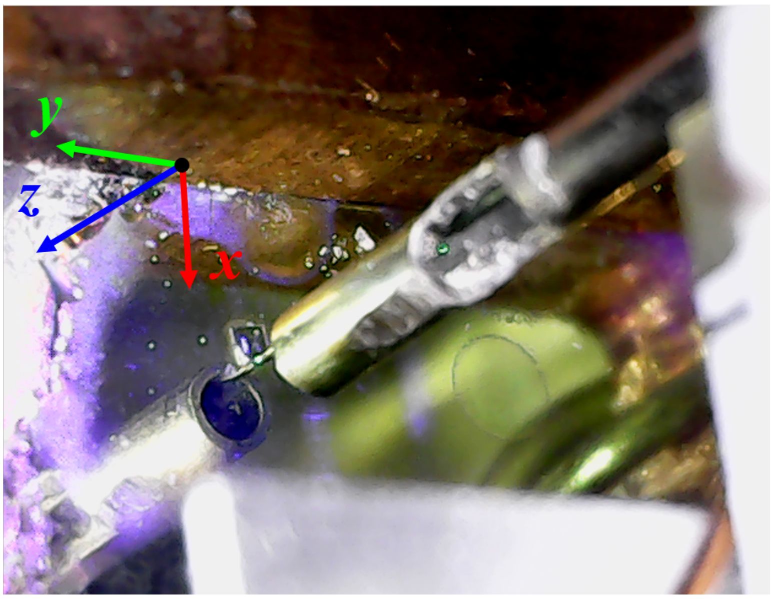

Figure 3.6: **A zoomed in picture of the microcavity taken by a microscope.** The geometry between the fiber and the mirror is shown.

The transmission of the cavity is collimated after the mirror and can then be either focused via free-space onto a photoiode[16] (PD) or an avalanche photodiode[17] (APD), or fiber-coupled to a spectrometer[18] or a single-photon counter[19].

3.1.5 Active Stabilization

In order to perform fluorescence spectroscopy in the cavity, an active stabilization scheme based on proportional-integral-derivative (PID) controllers is used[29]. A fast PID controller locks the cavity transmission to a flank of the resonance peak by outputting a control signal onto the fine z-piezo. Another slow PID controller locks the output of the fast PID controller to zero. By using a dichroic mirror[20], while the excitation laser at 532 nm is measured by the PD to lock the cavity, the fluorescence can be further sent to another detector or the spectrometer.

For quick measurements in the range of 10 s, a manual stabilization is more convenient. By manually tuning the voltage of the fine z-piezo, the cavity can be stabilized at the resonance peak.

---

[16] Thorlabs, PDA36A-EC

[17] Thorlabs, APD130A2/M

[18] Andor, SR-500i-D2-R-SIL

[19] Laser Components, Count-50C

[20] Semrock, FF552-Di02-25x36

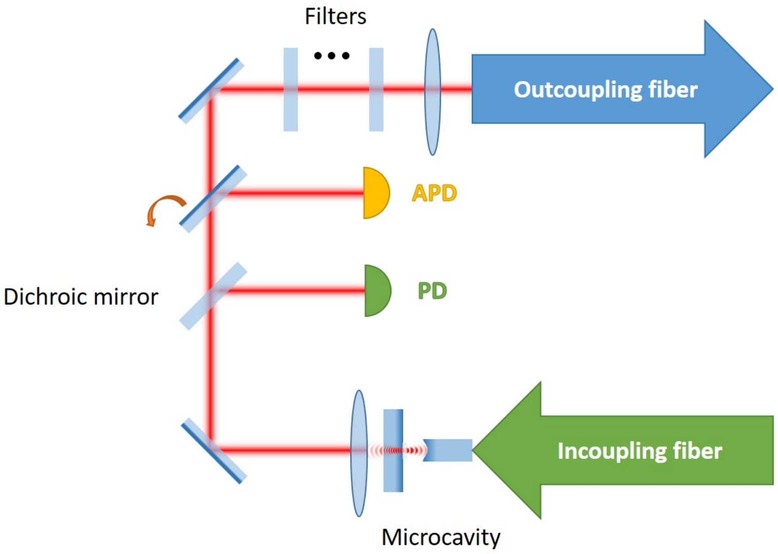

Figure 3.7: **Optical setup for the cavity measurement.**

3.2 Measurement Scheme

In such a scanning microcavity, a variety of measurements can be carried out. Examples are transmission, finesse, fluorescence and mode dispersion.

3.2.1 Cavity Resonance Spectrum

The cavity resonance spectrum can be measured by sweeping the coarse z-piezo voltage and recording the transmission signal via the PD or the APD. An example of cavity resonance measured on a clean part of the mirror is shown in Fig. 3.8. The higher peaks are the fundamental modes while the lower peaks are the higher-order modes. Assuming a linear response of the piezo, the distance between two adjacent fundamental modes is one FSR. The higher-order modes can be suppressed or even eliminated by adjusting the tilt of the fiber with respect to the mirror. By fitting the resonance peaks to Lorentzian lines, the finesse can be calculated. For example, in Fig. 3.8, the finesse is about 6000.

3.2.2 Cavity Scan

To determine the topology of the sample, a transversal cavity scan is carried out. In this case, the cavity works as a scanning cavity microscope. A number of different measurement schemes can be utilized while scanning the fiber across the mirror with x- and y-piezos, among which, the most straight forward measurement scheme is

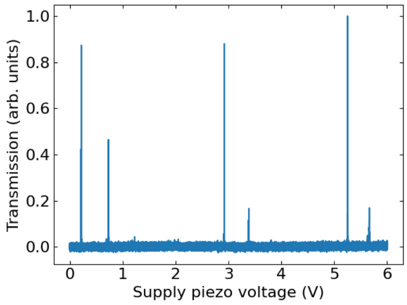

Figure 3.8: **Cavity resonance spectrum on a clean part of the mirror.** The piezo voltage is swept with a triangular waveform, and the actual change in cavity length depends on the piezoelectric coefficient and the linearity of the piezo.

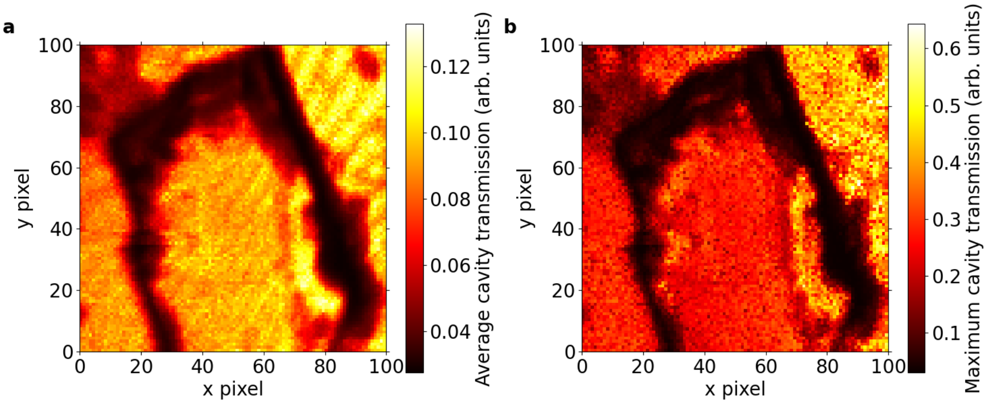

Figure 3.9: **Cavity transmission maps measured with 532 nm laser. a:** The average cavity transmission is taken for each point. **b:** The maximum cavity transmission is taken for each point.

the cavity transmission.

At each point of the transversal scan, a cavity resonance spectrum is measured and stored. To plot a cavity transmission map, either the maximum or average transmission of each point can be taken. Examples of both data evaluation methods based on the same cavity scan measurement are shown in Fig. 3.9, where the crystal in Fig. 3.12a is investigated. From the comparison, the average cavity transmission shows a higher contrast and signal to noise ratio. Therefore, all other cavity transmission maps will be shown as the average transmission.

In addition to cavity transmission map, the scanning cavity microscope can also be used to measure finesse maps, fluorescence maps, extinction spectroscopy and Raman spectroscopy.[27]

3.2.3 Cavity Mode Dispersion

The cavity mode dispersion is important for choosing a good cavity mode and cavity length for spectroscopic measurements. In addition, it determines the thickness, the refractive index and the birefringence of the crystal.

To measure the cavity mode dispersion, the broadband laser is coupled into the cavity and the transmission is coupled to the spectrometer and the spectra are recorded for each cavity length controlled by the coarse z-piezo. The transverse position of the fiber is fixed over the crystal.

In addition to the broadband laser, the fluorescence from the sample in the cavity can also be used to measure the mode dispersion. In this case, it is called the emission dispersion. With broadband emission ($\sim$ 100 nm), the emission dispersion of color centers in diamond can be easily measured.[58]. However, in the case of europium-embedded molecular complexes, the emission consists of several isolated lines, with corresponding linewidths of less than 1 nm, as shown in Fig. 3.14. Therefore the emission dispersion can not reveal the cavity mode dispersion throughout the entire spectral range, but it can still reveal how much emission is coupled into the cavity modes.

3.3 Sample Preparation

To achieve cavity enhancement, we integrate the Eu^{3+}-embedded molecular complexes into the microcavity via crystallization from a solution. The optical and spectroscopic properties of the crystals are characterized after the process.

3.3.1 Molecular Structure

The material we use is a molecular mononuclear Eu^{3+} complex $[Eu(BA)_4(pip)]$, where BA and pip stands for benzoylacetonate and piperidin-1-ium, respectively [59]. The structure of the molecule is shown in Fig. 3.10. This molecule has been recently shown to posses an ultra-narrow homogeneous linewidth of 4.6 kHz and long optical coherence time of 68 μs[17], after diluted to 5%. The refractive index of such molecule in crystalline form is assumed to be 1.5[17], but there is no measurement so far.

By engineering the molecular structures, the transition amplitudes and the interaction between qubits can be modified, as discussed in Sec. 2.1.3.

3.3.2 Crystallization on Cavity Mirror

The molecular complex is typically synthesized in the form of powders. For recrystallization, we dissolve 100 mg of the powder into 5 ml ethanol to form a saturated

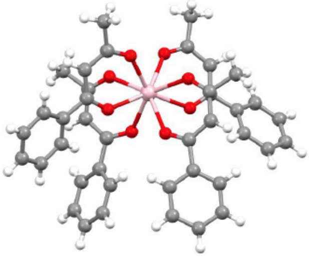

Figure 3.10: **Structure of the molecular mononuclear Eu^{3+} complex.** Grey, carbon; white, hydrogen; pink, europium; red, oxygen. The figure is taken from Ref. [17]

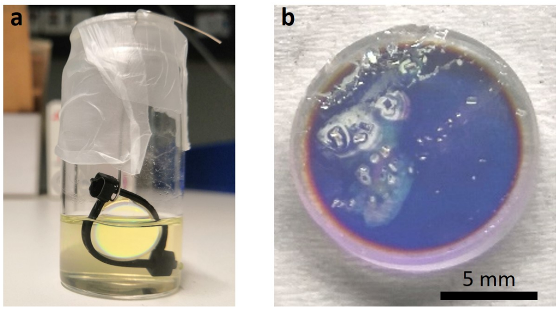

Figure 3.11: **Crystal growth on a cavity mirror. a**: The cavity mirror is hung half way into the solution. The bottle is sealed but left with holes on top. **b**: The cavity mirror after recrystallization process.

solution at room temperature. Then the cavity mirror is hung half way into the solution, an example is shown in Fig. 3.11a. The entire mirror is then coated by a thin layer of solution due to capillarity effect. The bottle is then sealed[21] with some ventilation holes on top to achieve a slow evaporation rate and protect foreign objects from falling in, reducing the chance of contamination. The solution takes roughly a week to vaporize, depending on the ambient temperature and humidity. After the solution level declines due to evaporation, leaving the entire mirror in the air, the crystallization process is completed. Good crystallization is achieved when a clean mirror with homogeneous distribution of crystals is obtained, as shown in Fig. 3.11b.

3.3.3 Characterization of the Crystals

After crystallization, the mirror is first put into a microscope to obtain information on the topology and location of the crystals. Some examples of the crystals are

---

[21] Parafilm M sealing film

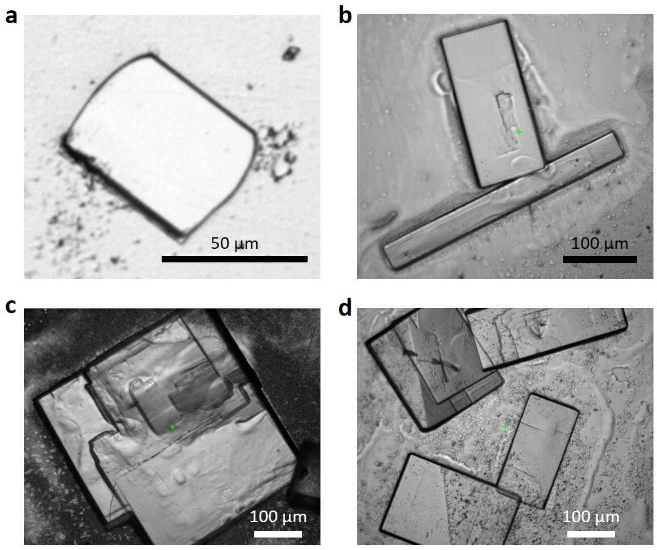

Figure 3.12: **Crystals under a microscope.** **a**: Small and thin crystal, with thickness around 2 μm and RMS surface roughness around 0.4 nm, which is ideal for cavity integration. **b**: Crystals with larger sizes. RMS surface roughnesses, about 0.7 nm, are good enough and very easy to localize in the cavity. The thickness is about 8 μm. **c**: Overgrown large crystal, which is not suitable for cavity due to bad surface roughness and large height. **d**: Crystals overlapping each other. Also not suitable for cavity integration because the crystal on top is tilted and the air gap between crystals has undesired effects on the cavity.

shown in Fig. 3.12.

The surface roughness of the crystals is then measured with the WLI. In addition, the height profile is obtained by reconstruction, from which the surface roughness can be determined. As an example, the interference pattern and the corresponding reconstructed height of the crystal in Fig. 3.12a is shown in Fig. 3.13a and b, respectively. To estimate the surface roughness, we calculate the RMS of the residuum by fitting a plane to the height profile. The RMS over an area of 5 μm $\times$ 5 μm is 0.4 nm. According to Eq. (2.41), this surface roughness correspond to scattering losses of 100 ppm. The geometry thickness of the crystal can also be measured by comparing the motor positions while focusing on the top of the crystal and the mirror. The thickness of the particular crystal shown in Fig. 3.13 is about 2 μm.

The fluorescence spectra are measured in a confocal setup with an off-resonant excitation. The results are shown in Fig. 3.14, and all the corresponding transitions are marked. The spectra are consistent to that in Ref. [17], which indicates that the molecular complex maintain the optical properties after recrystallization such as linewidths and resonance wavelengths.

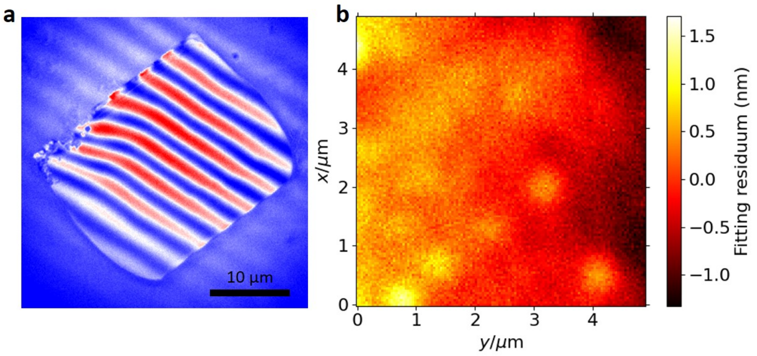

Figure 3.13: **Interference pattern and profile reconstruction.** **a**: Interference pattern measured with WLI. **b**: Height profile of the crystal from reconstruction. The profile is fitted to a plane and here the residuum is shown.

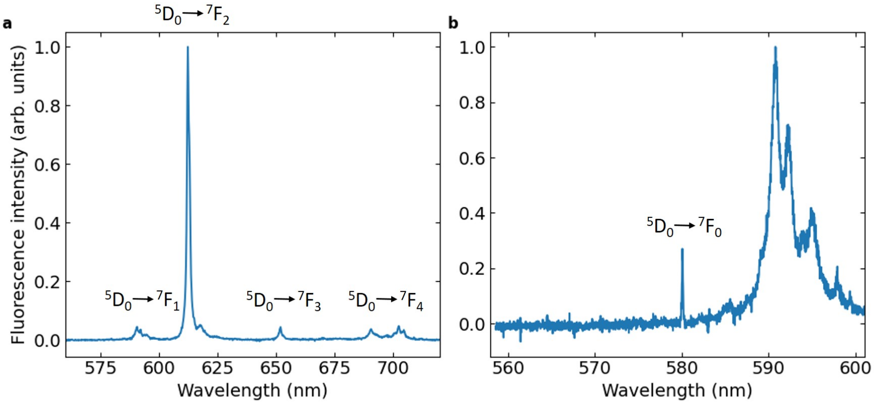

Figure 3.14: **Fluorescence spectra of crystals from a confocal setup, with excitation at 532 nm.** The optical transitions discussed in Sec. 2.1.3 are labeled in the spectra. **a**: Spectrum with low resolution: The spectrum features a strong transition near 613 nm. **b**: Spectrum with high resolution: The sharp peak at 580 nm with a linewidth of 0.17 nm corresponds to $^5D_0 \rightarrow {}^7F_0$ transition, which is also used for resonant excitation. The measurement limit of the spectrometer is below 0.07 nm.

Chapter 4

Results and Discussion

In this chapter, we demonstrate the cavity operation with integrated molecular crystals. A number of measurement results are shown and discussed.

4.1 Cavity Performance

Before doing spectroscopy, we first characterize the performance of the cavity, in order to estimate the thickness of the crystals and the losses introduced by the crystals. Most importantly, we search for an ideal location for spectroscopy measurements.

4.1.1 Scanning Cavity Microscopy of Molecular Crystals

Before the measurement on a particular crystal, the cavity is first aligned and then characterized at a clean part of the mirror, after which, a finesse of about 10,000 is measured. The actual finesse is lower than the design value of 28,000 because of additional loss channels like absorption or scattering losses introduced by e.g. solution residues.

With the help of the two motors the cavity mirror can be precisely driven to any crystal position. This can be confirmed by comparing the shape of the crystal in the cavity scan to that in the WLI. An image from a microscope[1] is shown in Fig. 4.1.

We first scan the cavity with the 532 nm excitation due to the high transmission which arises from this wavelength being located at the edge of the stop band. The cavity transmission map is shown in Fig. 4.2a, where the topology of the crystal can

---

[1] Reflecta DigiMicroscope USB 200

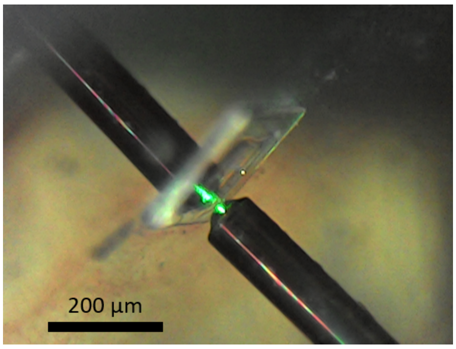

Figure 4.1: **Image of a crystal in the cavity.** The lower part is the single-mode fiber with a laser-machined end facet and the upper part is the mirror image of it. The diameter of the fiber is about 125 μm.

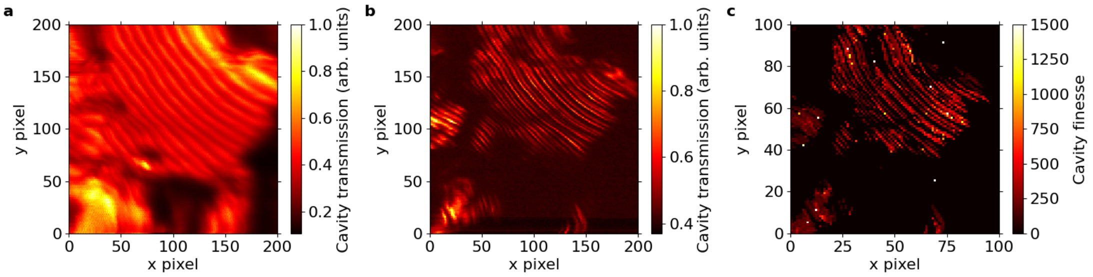

Figure 4.2: **Scanning cavity microscopy on a crystal.** All the three measurements have the same scan range of about 70 μm × 70 μm. **a**: Transmission map measured with 532 nm excitation. **b**: Transmission map measured with 580 nm excitation. **c**: Finesse map measured with 580 nm excitation. This scan has a lower resolution than the other two.

be seen. The stripe-like structures indicate an alternating air-like and dielectric-like modes due to the change of the crystal height at the surface.[28] To determine which mode has a higher transmission, we investigate the mode dispersion in more details in the next section.

Then, the transmission map with 580 nm excitation is measured, as shown in Fig. 4.2b. By comparison, it is evident that forming a cavity with 532 nm excitation is simpler than with 580 nm excitation, but results in a lower contrast.

To measure the finesse map with 580 nm excitation, two measurements are taken at each pixel in the cavity scan and the average value is plotted in Fig. 4.2c. If no cavity is formed, the finesse will be treated as zero. The consistency between the finesse map and the transmission map allows us to use the transmission as an indication of the finesse. On a thin and smooth crystal, a finesse of up to 4,000 can

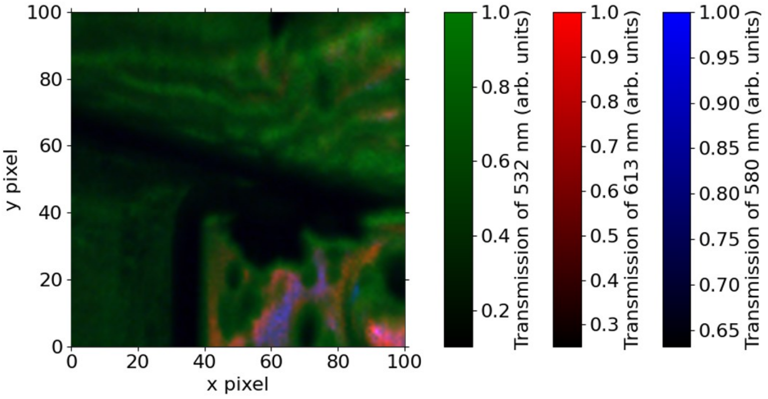

Figure 4.3: **Multi-channel scanning cavity microscopy.** Outputs at 532 nm, 613 nm and 580 nm from the AOTF are used.

be measured with 580 nm excitation.

Using the output from the AOTF, we can perform scanning cavity microscopy with any excitation wavelength. As shown in Fig. 4.3, three cavity scans with 532 nm, 613 nm and 580 nm excitation are measured separately and merged together. With the multi-channel scan, the cavity performance with different wavelengths can be compared. In the lower-right part of the scan, all three wavelengths show high transmission, which indicates an ideal location for fluorescence spectroscopy.

4.1.2 Mode Dispersion of a Hybrid Cavity

Using the method described in Sec. 3.2.3, the cavity mode dispersion is measured with the broadband laser, as shown in Fig. 4.4a and b. In general, the fundamental modes are dominant, but the higher-order modes become visible occasionally as the alignment of the cavity fiber varies for different wavelengths and cavity lengths. The anti-crossing behavior, shown in Fig. 2.12, is also observed. By connecting those points which are air-like, the pure air modes can be reconstructed. From Fig. 2.12b, the vertical distance between two reconstructed pure air modes is about 12.5 nm, which corresponds to an air gap of 13 μm according to Eq. (2.21).

From the mode dispersion measurement, we find out that air-like and dielectric-like modes have different transmissions. The dielectric-like modes, with shallower slopes, show higher transmission than the air-like modes.

The dielectric-like modes having higher transmission indicates that the dielectric-cavity has a higher finesse. One factor is that the crystal grown on top of the mirror coating will change the transmittance. According to our simulation of the hybrid cavity, the transmittance reduces from 200 ppm to 150 ppm, which will increase

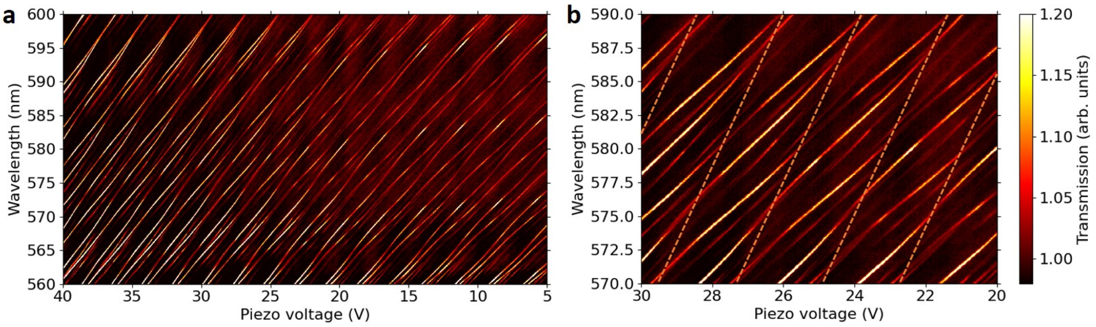

Figure 4.4: **Mode dispersion of a hybrid cavity.** A higher piezo voltage means a shorter cavity length. First, the transmission at each wavelength is calibrated with respect to the average of all cavity lengths. Then for each cavity length, the spectrum is normalized to the maximum. **a**: A measurement with a piezo voltage range of 40 V, corresponding to a cavity length change of about 2 μm. **b**: A zoomed in region of **a**. Alternating air-like and dielectric-like modes can be seen more clearly here. An air-like mode has a steeper slope and a lower transmission. The orange lines show the reconstructed pure air modes by connecting the points which are air-like, with steeper slope and lower transmission.

the finesse of the dielectric-cavity. The concave profile on the fiber end facet could also contribute to a lower finesse of the air-cavity. The mode hybridization could be different from case to case. In a recent research [28] dealing with diamond membranes in such a microcavity, the air-like modes have higher transmission due to losses at the diamond membrane.

4.1.3 Emission Dispersion

Similar to the mode dispersion, the same scheme can be used to measure the emission dispersion. In this case, the 532 nm laser is coupled into the cavity. The resulting emission dispersion is shown in Fig. 4.5a. While sweeping the cavity length, the emission can be observed when the cavity is resonant to the excitation. However, the broadband emission will normally be coupled into several cavity modes, as seen in the left part of Fig. 4.5a. When the cavity is well aligned and only one fundamental mode is resonant to the emission, the emission is significantly enhanced, as seen in the right part of Fig. 4.5a. The integrated fluorescence intensity shown in Fig. 4.5b demonstrates the dependency of the emission on the cavity length

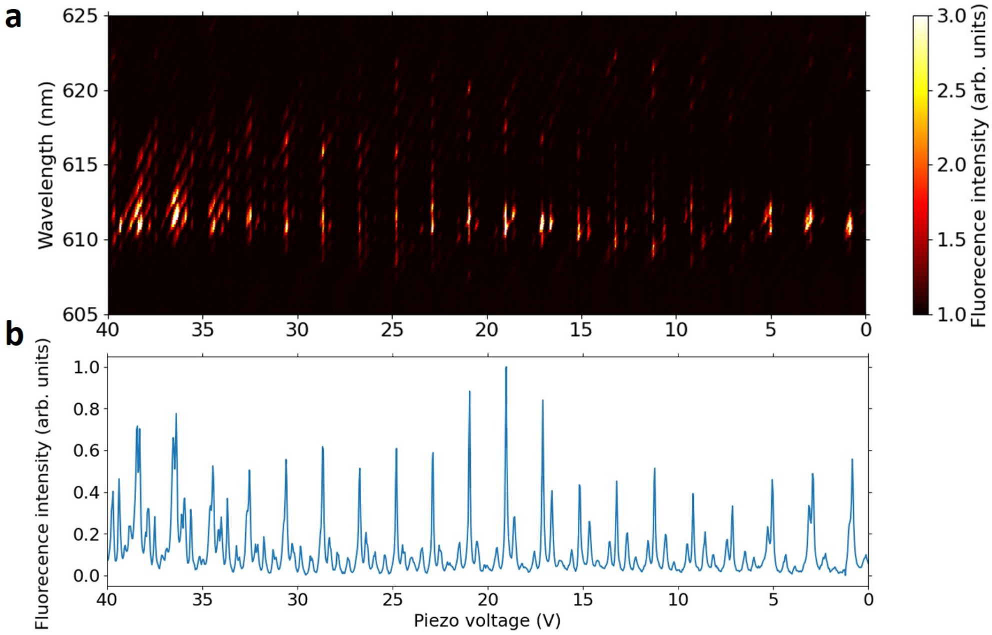

Figure 4.5: **Emission dispersion near 613 nm.** The excitation is at 532 nm. **a**: Emission spectra at different piezo voltages. Only cavity lengths resonant to the excitation can produce emission, which will be further coupled to several cavity modes. When the emission is also resonant to a fundamental cavity mode, a sharp and high emission line can be observed. **b**: Integrated fluorescence intensity from 605 nm to 625 nm.

4.2 Cavity Fluorescence Spectroscopy

Different from the fluorescence spectroscopy in free-space, the sample fluorescence in the cavity cannot be fully coupled out. Only those which are resonant to the cavity modes can be collected. Therefore the so-called double resonance condition has to be fulfilled.

4.2.1 Double Resonance Condition

The emitted fluorescence is only measurable when the cavity is resonant to both the excitation and fluorescence, which is in this particular case at about 1 V in Fig. 4.5. We call this the double resonance condition.

To find the double resonance condition, 532 nm and 613 nm excitation light with a bandwidth of 1 nm from the AOTF output are simultaneously coupled into the cavity. The transmission of the two wavelengths are split by using a dichroic mirror with cut-off wavelength of 552 nm and the corresponding signals can be detected

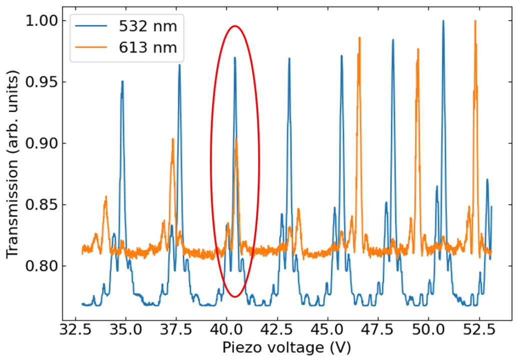

Figure 4.6: **Resonance spectrum of a two-color cavity.** The double resonance condition is fulfilled for the highlighted mode.

by the PD and the APD, respectively. The cavity resonance spectra for both wavelengths are shown in Fig. 4.6.

4.2.2 Fluorescence Spectroscopy

To measure the fluorescence spectrum, the cavity is actively locked to the 532 nm transmission using the method described in Sec. 3.1.5. After a notch filter[2], the fluorescence is coupled to the spectrometer. The fluorescence spectra when the cavity is locked at a series of adjacent longitudinal cavity modes with 532 nm excitation are shown in Fig. 4.7. A significant enhancement is observed when the double resonance condition is fulfilled, as shown by the green spectrum.

4.3 Measuring the Purcell Effect

In order to determine a Purcell factor, an off-resonant pulsed excitation scheme was used to measure the lifetime in the cavity and then compared to the free-space lifetime.

4.3.1 Estimation of the Purcell Factor

With the cavity mode dispersion and the finesse measurements on the crystal, it becomes possible to estimate the Purcell factor. From Fig. 4.4, the FSR in wavelength domain near 580 nm is about 6 nm, which indicates an optical cavity

---

[2] Semrock NF03-532E-25

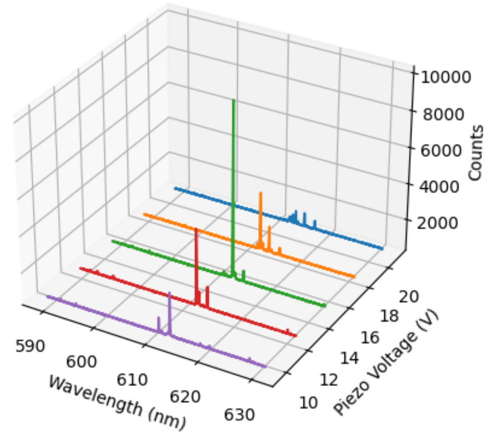

Figure 4.7: **Fluorescence spectra of different longitudinal modes.** The emission is significantly enhanced when the double resonance condition is fulfilled, as shown by the green spectrum. The exposure time is 1 s.

length of 28 μm, according to Eq. (2.21). Then it follows that the mode order

$$q = \frac{2l}{\lambda} = 97. \tag{4.1}$$

This cavity length is different from the air gap calculated before. Here the optical thickness of the crystal is also included. By comparing the air gap and optical cavity length, we can find the optical thickness of the crystal is 15 μm, corresponding to a geometric thickness of 10 μm. This is close to the geometric thickness of 8 μm measured in the WLI.

Since 580 nm and 613 nm are both within the stop band and are of similar wavelengths, the Q-factor with 580 nm excitation can be used to approximate the Q-factor with 613 nm excitation. Taking the finesse with 580 nm excitation to be 4,000, then according to Eq. (2.45), the Q-factor of the cavity is

$$Q_\mathrm{c} = q\mathcal{F} = 388,000. \tag{4.2}$$

From the fluorescence spectrum measured in the confocal setup (see Fig. 3.14), the linewidth of the $^5\mathrm{D}_0 \rightarrow {}^7\mathrm{F}_2$ emission at 613 nm is estimated to be 1.5 nm, and thus the Q-factor of the emitter is

$$Q_\mathrm{em} = \frac{\lambda}{\delta\lambda} = 409. \tag{4.3}$$

Since the Q-factor of the cavity is much higher than that of the emitter, the effective Q-factor in Eq. (2.83) has a dominant contribution from the Q-factor of the emitter, i.e. $Q_\mathrm{eff} \approx Q_\mathrm{em} = 409$.

The mode volume V_{m} can be calculated from the geometry of the cavity as follows. The wavefront of the fundamental Gaussian mode should match the profile of the fiber end facet. In Eq. (2.36), z is set as the cavity length 28 μm and $R(z)$ be the radius of curvature of the fiber end facet 40 μm, then the Rayleigh range z_0 can be calculated as

$$z_0 = z\sqrt{\frac{R(z)}{z} - 1} = 18.3\ \mu\mathrm{m}. \tag{4.4}$$

Then, according to Eq. (2.34) and (2.47), the mode volume V_{m} is

$$V_{\mathrm{m}} = \frac{\lambda l z_0}{4} = 79\ \mu\mathrm{m}^3. \tag{4.5}$$

Finally, using Eq. (2.84), we obtain a Purcell factor of $C = 0.09$.

The estimated Purcell factor highly depends on the emission linewidth at 613 nm and the cavity length. In addition, using the finesse at 580 nm will overestimate the Q-factor at 613 nm because the DBR coating is designed to have the maximum reflectivity at 585 nm, which is closer to 580 nm.

According to the estimated Purcell factor, the cavity provides an extra 9% emission rate into the cavity mode, from which a lifetime shortening of 9% is expected. However, the majority of the emission is still emitted into the free-space modes.

4.3.2 Pulsed Excitation

To achieve pulsed excitation, the simplest solution is to use a semicircular chopper wheel, with an on-off modulation of the laser and a duty cycle of 50% at a frequency up to 100 Hz. The transmission is coupled to the single-photon counter. To characterize the chopper wheel, the total transmission, mostly the excitation laser, is sent to the single-photon counter after a neutral density filter with a sufficient optical density avoiding saturation of the detector. The transient of the chopper wheel is shown in Fig. 4.8. At a rotation speed of about 40 Hz, the falling time is about 50 μs.

4.3.3 Lifetime Shortening

With off-resonant pulsed excitation at 532 nm, the optical lifetime can be measured by fiber-coupling the fluorescence from the cavity to the single-photon counter. To compare the lifetimes in a confocal setup and in the cavity, identical pulse sequences are sent to both setups with crystals grown using the same method. The lifetimes measured in the cavity and the confocal setup are compared in Fig. 4.9.

As expected, the lifetime in the cavity highly depends on the location on the crystal and the cavity length. According to the statistics, the lifetimes in the cavity average

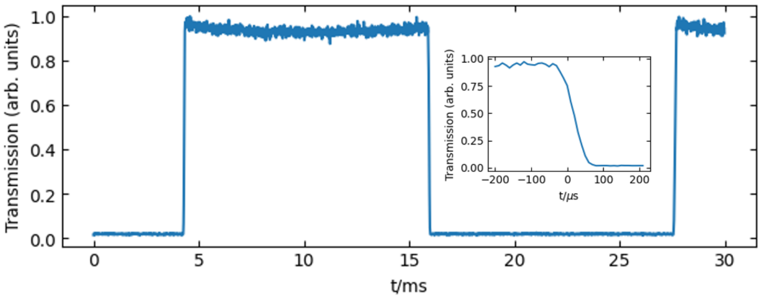

Figure 4.8: **The transient signal of the chopper wheel.** The inset shows the zoom of the falling edge. In this case, the falling time is about 50 μs, which is sufficient to measure an optical lifetime of 500 μs. The rotation speed is about 40 Hz.

526 ± 60 μs and those in the confocal setup average 532 ± 30 μs, compared to 540 μs measured in an ensemble at 1.45 K in Ref.[17]. The consistency of the free-space lifetime proves that our recrystallization method preserves the optical lifetime. The difference between cavity and free-space lifetime is within the statistic error. Therefore, we cannot conclude whether there is Purcell enhancement or not. However, since each data point is measured at a different location, it is reasonable to look at individual data points from the cavity measurements, and a few of them show a lifetime shortening of more than 10%.

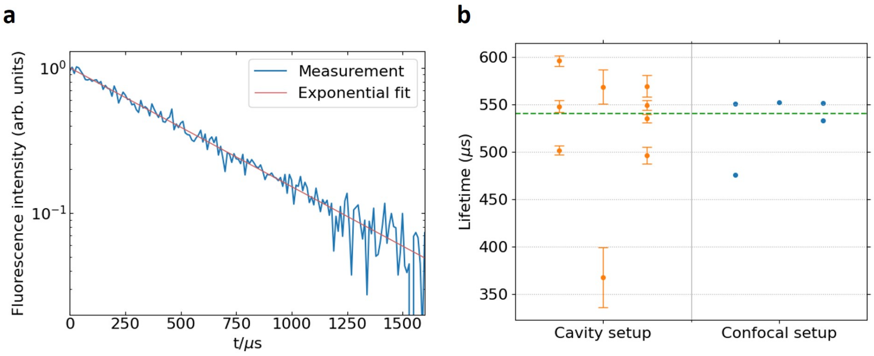

Figure 4.9: **Comparison of the lifetimes in confocal setup and in cavity. a:** An example of lifetime measurement in cavity. The exponential fit gives a lifetime of 531±6 μs. **b:** Data point distribution of the measurements in the cavity and the confocal setup. The orange points on the left side show the lifetimes measured in the cavity and the blue points on the right show the lifetimes measured in the confocal setup. As a reference, the green dashed line shows the lifetime of 540 μs measured in an ensemble at 1.45 K in Ref.[17]. The fitting errors of the confocal measurements are all below 1 nm, which is too small to demonstrate in the figure.

Chapter 5

Conclusion and Outlook

In this work, we integrate a newly synthesized Eu^{3+}-embedded molecular complex in the form of crystalline platelets into a microcavity and prove the cavity operation at room temperature. This work paves the way to cavity-enhanced spectroscopy at cryogenic temperatures of molecular complexes and to optically addressable qubits distributed in a microcavity.

With the reproducible crystallization method, we achieve thin crystals with thicknesses as low as 2 μm. The surface roughness RMS over an area of 5 μm $\times$ 5 μm is determined to be as low as 0.4 nm, which enables cavity operation with finesse as high as 4,000. The density of the crystals can also be controlled such that it is always possible to find a good crystal in the center of the mirror and that the crystals are not stacked together resulting in additional effects.

We perform a number of different measurements to characterize the hybrid cavity, including transmission maps, finesse maps, cavity mode dispersion and emission dispersion. In the next step, other measurements, like cavity extinction spectroscopy, can be tried out.

For the majority of crystals, a cavity can be formed with 580 nm excitation, which can be further used for resonant excitation. Based on the transmission and finesse maps, we can find suitable locations for ensemble spectroscopy measurements in the cavity.

Using a broadband laser, the cavity mode dispersion is measured, which shows the coupling between an air-cavity and a dielectric-cavity. With the help of simulations, the behavior of a hybrid cavity can be explained. The characteristics of the hybrid cavity depend on which cavity is in resonance. Thus, the hybrid cavity periodically change between an air-like cavity and a dielectric-like cavity. Those characteristics include transmission, finesse and dispersion behavior.

According to the dispersion measurements, the mode volume is below 100 μm^3, which still has further room to improve if the air gap is carefully monitored while approaching the crystal.

Using the emission dispersion and multichromatic transmission maps, locations fulfilling the double resonance condition are found. The cavity-enhanced fluorescence is measured using an active stabilization scheme. In order to measure the optical lifetime in the cavity and further to determine the Purcell factor, we use off-resonant pulsed excitation. The estimated Purcell factor is 0.09, corresponding to a lifetime shortening of 9%. Some measurements in the caivty show a reduction of around 10%, compared to free-space lifetime of 540 μs, but there is not yet a statistically convincing conclusion as the lifetime difference lies within the error.

At room temperature, the emission from $^5D_0 \rightarrow {}^7F_2$ transition is very broad, featuring a linewidth of more than 1 nm, resulting in a bad-emitter regime. The Purcell enhancement only comes from the spatial confinement. However, using resonant excitation scheme at liquid He temperature or 4.2 K, the linewidth of $^5D_0 \rightarrow {}^7F_0$ transition for an individual emitter is below 200 kHz[17]. Therefore, using resonant excitation at cryogenic temperatures can benefit from an emitter linewidth which is 7 orders of magnitude narrower, compared to off-resonant excitation at room temperature. In addition, for the resonant excitation scheme, no double resonance condition is required, and thus a high finesse can be achieved for both excitation and emission.

Looking into the future of quantum computing. The molecular complexes can be engineered to become bright emitters with excellent coherence properties. Multiple ions can be embedded into one molecule, resulting in multi-qubit coupling with defined strength. The ability to form thin and smooth crystalline structures makes the molecular complexes scalable. Such optically addressable qubits can be distributed on a mirror, becoming a “quantum chip”. Furthermore, nanosturctures can also be implemented onto the “chip”, creating connections between qubits in large scale.

Bibliography

[1] A. L. Schawlow and C. H. Townes. “Infrared and optical masers”. In: *Physical review* 112.6 (1958), p. 1940.

[2] F. Krausz and M. Ivanov. “Attosecond physics”. In: *Reviews of modern physics* 81.1 (2009), p. 163.

[3] F. Jazaeri et al. “A review on quantum computing: From qubits to front-end electronics and cryogenic MOSFET physics”. In: *2019 MIXDES-26th International Conference" Mixed Design of Integrated Circuits and Systems"*. IEEE. 2019, pp. 15–25.

[4] S. Welinski et al. “Coherence time extension by large-scale optical spin polarization in a rare-earth doped crystal”. In: *Physical Review X* 10.3 (2020), p. 031060.

[5] C. D. Bruzewicz et al. “Trapped-ion quantum computing: Progress and challenges”. In: *Applied Physics Reviews* 6.2 (2019).

[6] V. Kaushal et al. “Shuttling-based trapped-ion quantum information processing”. In: *AVS Quantum Science* 2.1 (2020).

[7] M. Saffman, T. G. Walker, and K. Mølmer. “Quantum information with Rydberg atoms”. In: *Reviews of modern physics* 82.3 (2010), p. 2313.

[8] C. S. Adams, J. D. Pritchard, and J. P. Shaffer. “Rydberg atom quantum technologies”. In: *Journal of Physics B: Atomic, Molecular and Optical Physics* 53.1 (2019), p. 012002.

[9] L. V. Rodgers et al. “Materials challenges for quantum technologies based on color centers in diamond”. In: *MRS Bulletin* 46.7 (2021), pp. 623–633.

[10] S. Pezzagna and J. Meijer. “Quantum computer based on color centers in diamond”. In: *Applied Physics Reviews* 8.1 (2021).

[11] A. Kinos et al. “Roadmap for rare-earth quantum computing”. In: *arXiv preprint arXiv:2103.15743* (2021).

[12] M. Grimm et al. “Universal quantum computing using electronuclear wavefunctions of rare-earth ions”. In: *Prx Quantum* 2.1 (2021), p. 010312.

[13] C. S. Lent and P. D. Tougaw. “A device architecture for computing with quantum dots”. In: *Proceedings of the IEEE* 85.4 (1997), pp. 541–557.

[14] C. Kloeffel and D. Loss. “Prospects for spin-based quantum computing in quantum dots”. In: *Annu. Rev. Condens. Matter Phys.* 4.1 (2013), pp. 51–81.

[15] M. Zhong et al. “Optically addressable nuclear spins in a solid with a six-hour coherence time”. In: *Nature* 517.7533 (2015), pp. 177–180.

[16] Z. W. Riedel et al. “Synthesis of Eu $(HCOO)_3$ and Eu $(HCOO)_3(HCONH_2)_2$ crystals and observation of their $^5D_0 \rightarrow {}^7F_0$ transition for quantum information systems”. In: *Journal of Luminescence* 249 (2022), p. 119006.

[17] D. Serrano et al. “Ultra-narrow optical linewidths in rare-earth molecular crystals”. In: *Nature* 603.7900 (2022), pp. 241–246.

[18] K. S. Kumar et al. “Optical spin-state polarization in a binuclear europium complex towards molecule-based coherent light-spin interfaces”. In: *Nature communications* 12.1 (2021), p. 2152.

[19] S. K. Kuppusamy et al. “Observation of Narrow Optical Homogeneous Linewidth and Long Nuclear Spin Lifetimes in a Prototypical [Eu (trensal)] Complex”. In: *The Journal of Physical Chemistry C* (2023).

[20] G. Rempe et al. “Measurement of ultralow losses in an optical interferometer”. In: *Optics letters* 17.5 (1992), pp. 363–365.

[21] H. Kelkar et al. “Sensing nanoparticles with a cantilever-based scannable optical cavity of low finesse and sub-λ^3 volume”. In: *Physical Review Applied* 4.5 (2015), p. 054010.

[22] D. Hunger et al. “Laser micro-fabrication of concave, low-roughness features in silica”. In: *Aip Advances* 2.1 (2012).

[23] J. P. Reithmaier et al. “Strong coupling in a single quantum dot–semiconductor microcavity system”. In: *Nature* 432.7014 (2004), pp. 197–200.

[24] J. D. Thompson et al. “Coupling a single trapped atom to a nanoscale optical cavity”. In: *Science* 340.6137 (2013), pp. 1202–1205.

[25] M. Trupke et al. “Microfabricated high-finesse optical cavity with open access and small volume”. In: *Applied Physics Letters* 87.21 (2005).

[26] M. Mader et al. “A scanning cavity microscope”. In: *Nature communications* 6.1 (2015), p. 7249.

[27] T. Hümmer et al. “Cavity-enhanced Raman microscopy of individual carbon nanotubes”. In: *Nature communications* 7.1 (2016), p. 12155.

[28] J. Körber et al. “Scanning cavity microscopy of a single-crystal diamond membrane”. In: *Physical Review Applied* 19.6 (2023), p. 064057.

[29] M. Pallmann et al. “A highly stable and fully tunable open microcavity platform at cryogenic temperatures”. In: *APL Photonics* 8.4 (2023).

[30] H. N. Russell and F. A. Saunders. “New regularities in the spectra of the alkaline earths”. In: *Astrophysical Journal, vol. 61, p. 38* 61 (1925), p. 38.

[31] O. Laporte and W. F. Meggers. “Some rules of spectral structure”. In: *Josa* 11.5 (1925), pp. 459–463.

[32] K. Binnemans. “Interpretation of europium (III) spectra”. In: *Coordination Chemistry Reviews* 295 (2015), pp. 1–45.

[33] A. Souza and M. C. Dos Santos. “The J-mixing effect in Ln^{3+} ions crystal field levels”. In: *Chemical Physics Letters* 521 (2012), pp. 138–141.

[34] J. Longdell, A. Alexander, and M. Sellars. “Characterization of the hyperfine interaction in europium-doped yttrium orthosilicate and europium chloride hexahydrate”. In: *Physical Review B* 74.19 (2006), p. 195101.

[35] K. M. Smith et al. “Complete crystal-field calculation of Zeeman hyperfine splittings in europium”. In: *Physical Review B* 105.12 (2022), p. 125141.

[36] A. Reiserer and G. Rempe. “Cavity-based quantum networks with single atoms and optical photons”. In: *Reviews of Modern Physics* 87.4 (2015), p. 1379.

[37] G. R. Guthöhrlein et al. “A single ion as a nanoscopic probe of an optical field”. In: *Nature* 414.6859 (2001), pp. 49–51.

[38] M. Keller et al. “Continuous generation of single photons with controlled waveform in an ion-trap cavity system”. In: *Nature* 431.7012 (2004), pp. 1075–1078.

[39] L. Kohler et al. “Tracking Brownian motion in three dimensions and characterization of individual nanoparticles using a fiber-based high-finesse microcavity”. In: *Nature Communications* 12.1 (2021), p. 6385.

[40] A. Trichet et al. “Nanoparticle trapping and characterization using open microcavities”. In: *Nano letters* 16.10 (2016), pp. 6172–6177.

[41] C. Vallance et al. “Open-access microcavities for chemical sensing”. In: *Nanotechnology* 27.27 (2016), p. 274003.

[42] H. Snijders et al. “Fiber-coupled cavity-QED source of identical single photons”. In: *Physical Review Applied* 9.3 (2018), p. 031002.

[43] C. Fabry. “Theorie et applications d’une nouvelle methods de spectroscopie intereferentielle”. In: *Ann. Chim. Ser. 7* 16 (1899), pp. 115–144.

[44] A. Perot and C. Fabry. “On the application of interference phenomena to the solution of various problems of spectroscopy and metrology”. In: *Astrophysical Journal, vol. 9, p. 87* 9 (1899), p. 87.

[45] *Gaussian Beam*. `https://en.wikipedia.org/wiki/Gaussian_beam`. Accessed: 2023-09-06.

[46] G. Vallone. "On the properties of circular beams: normalization, Laguerre–Gauss expansion, and free-space divergence". In: *Optics letters* 40.8 (2015), pp. 1717–1720.

[47] M. A. Bandres and J. C. Gutiérrez-Vega. "Ince–gaussian beams". In: *Optics letters* 29.2 (2004), pp. 144–146.

[48] H. Bennett and J. Porteus. "Relation between surface roughness and specular reflectance at normal incidence". In: *JOSA* 51.2 (1961), pp. 123–129.

[49] S. B. Van Dam, M. Ruf, and R. Hanson. "Optimal design of diamond-air microcavities for quantum networks using an analytical approach". In: *New Journal of Physics* 20.11 (2018), p. 115004.

[50] E. Janitz et al. "Fabry-Perot microcavity for diamond-based photonics". In: *Physical Review A* 92.4 (2015), p. 043844.

[51] S. Bogdanović et al. "Design and low-temperature characterization of a tunable microcavity for diamond-based quantum networks". In: *Applied Physics Letters* 110.17 (2017).

[52] S. A. Furman and A. V. Tikhonravov. *Basics of optics of multilayer systems*. Atlantica Séguier Frontieres, 1992.

[53] H. Choi, M. Heuck, and D. Englund. "Self-similar nanocavity design with ultrasmall mode volume for single-photon nonlinearities". In: *Physical review letters* 118.22 (2017), p. 223605.

[54] E. M. Purcell, H. C. Torrey, and R. V. Pound. "Resonance absorption by nuclear magnetic moments in a solid". In: *Physical review* 69.1-2 (1946), p. 37.

[55] C. J. R. Sheppard. "Approximate calculation of the reflection coefficient from a stratified medium". In: *Pure and Applied Optics: Journal of the European Optical Society Part A* 4.5 (1995), p. 665.

[56] W. Sellmeier. "III. Ueber die durch die Aetherschwingungen erregten Mitschwingungen der Körpertheilchen und deren Rückwirkung auf die erstern, besonders zur Erklärung der Dispersion und ihrer Anomalien". In: *Annalen der Physik* 221.3 (1872), pp. 399–421.

[57] T. Hümmer. "Cavity-enhanced Hyperspectral Raman and Absorption Microscopy". PhD thesis. lmu, 2019.

[58] M. Pallmann. "Purcell-enhanced emission and collective effects of nitrogen-vacancy centers in diamond coupled to a microcavity". PhD thesis. Dissertation, Karlsruhe, Karlsruher Institut für Technologie (KIT), 2023.

[59] C. Toninelli et al. “Single organic molecules for photonic quantum technologies”. In: *Nature Materials* 20.12 (2021), pp. 1615–1628.